

# Physical mechanisms of non-seismic phenomena accompanying earthquakes: An Overview

<sup>1,2</sup>V. V. Surkov

<sup>1</sup>Institute of Physics of the  
Earth RAS, Moscow

<sup>2</sup>IZMIRAN, Troitsk, Moscow



## **Introduction**

### **1. Local changes in the rock basement conductivity**

1.1. Effect of conductive groundwater

1.2. Changes in the rock conductivity under influence of tectonic strain

### **2. Abnormal ULF electromagnetic noise possibly related to earthquakes**

2.1. Rock electization due to the generation of microcracks

2.2. Perturbations of geomagnetic field caused by acoustic emission of cracks situated in conducting rocks

2.3. Electrokinetic effect in porous water-saturated rocks

### **3. Co-seismic electromagnetic phenomena**

3.1. Seismoelectric effect

3.2. Geomagnetic field perturbations caused by seismic waves in conductive ground

3.3. Effect of acoustic-gravity waves on the ionosphere

### **4. Atmospheric effects due to gas and aerosols emission from soil**

4.1. Radon effect on the atmospheric conductivity

4.2. Abnormal IR radiation from the atmosphere observed above seismo-active regions

### **5. Ionospheric effects due to gas and aerosols emission from soil**

5.1. Whether the radon emission from soil can heat up the atmosphere?

5.2. Whether seismogenic atmospheric current can have an effect on the ionosphere?

### **6. Conclusion**

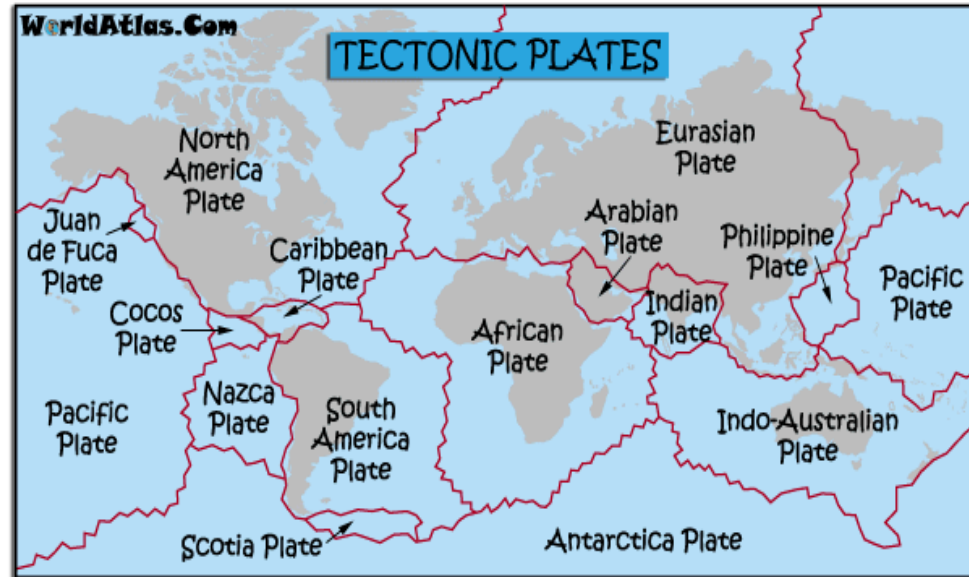


**Fig. 1.** Tectonics of lithospheric plates

Since the discovery of tectonic plate motion several decades ago, the short-term prediction problem can be seemingly solved for a short time. At the time being it is clear that the tectonic plate dynamics can predict only a possibility of EQ occurrence on the geological time scale (10–100 years) that may offer long-term prediction, but nothing tells about short-term EQ prediction. Foreshocks and other seismic precursors of EQs are very sporadic in nature, sometimes they appear before the quakes and sometimes they are absent at all.

# 1. Local changes in the rock basement conductivity

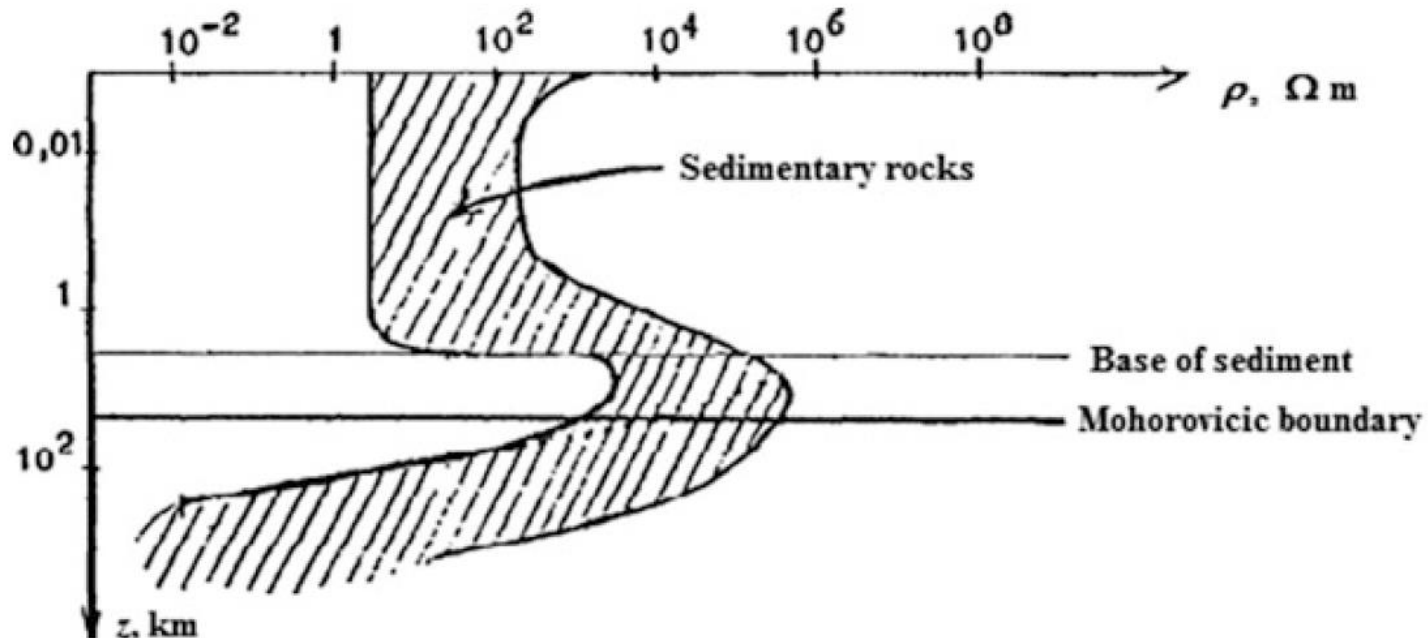


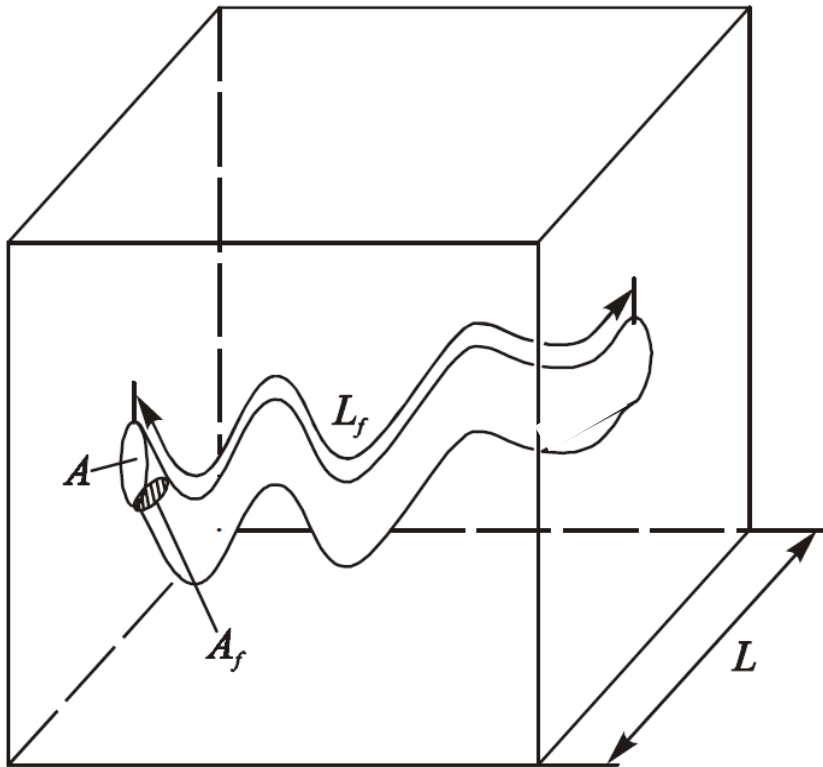
**Fig. 2.** Variations of the ground-specific resistance with depth as observed in the continental landmass. Adapted from Schwarz (1990)

Long-term observations in seismo-active regions have shown that the variations of the rock basement conductivity can be generated synchronously with an enhancement of seismic activity several months before and after the EQ occurrence

[Myachkin et al. 1972; Sobolev et al. 1972; Sobolev 1975; Rikitake and Yamazaki 1978; Honkura 1981; Rikitake 1987; Meyer and Teisseyre 1989; Park and Fitterman 1990; Park 1991; Bragin et al. 1992].

For example, Rikitake and Yamazaki (1978) observed the gradual decrease in the ground conductivity down to several percent several hours before the main shock in 21 cases among 30 ones when the considered effect was observed.

## 1.1. Effect of conductive groundwater



The electrical conductivity of dry rocks is much less than the electrical conductivity of groundwater. Therefore, the conductivity of the actual medium is almost completely determined by the percentage of groundwater content. The most probable reason for the change in electrical conductivity is associated with the effect of rock dilatancy and fluid diffusion through pore channels [Scholz et al., 1973].

**Fig. 3.** Capillary model a porous medium. A bunch of sinuous channels starting on one side of the sample and exiting on the other side is shown.

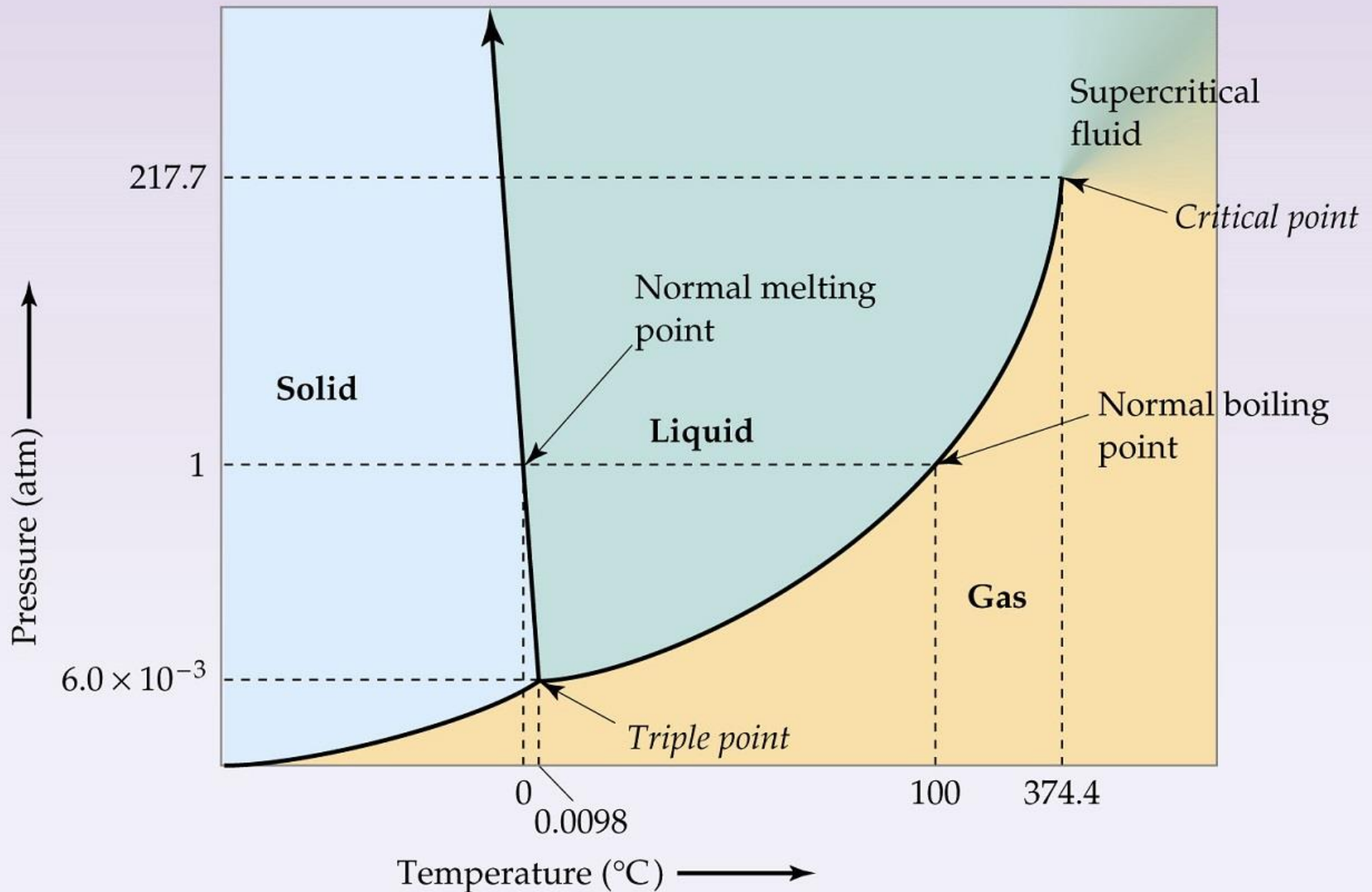


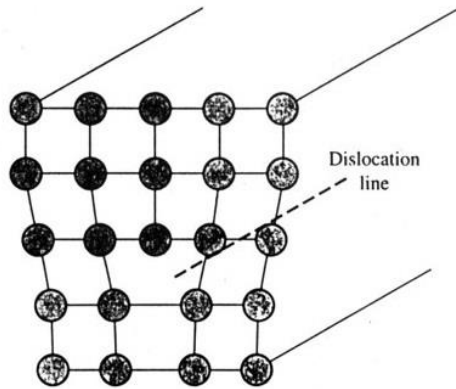
**Fig. 4.** Phase diagram of water

$$\Delta T = 0.02 \text{ grad/m} \times 3 \cdot 10^4 \text{ m} = 600^\circ\text{C} \quad \Delta P = \rho g h = 6 \cdot 10^8 \text{ Pa}$$

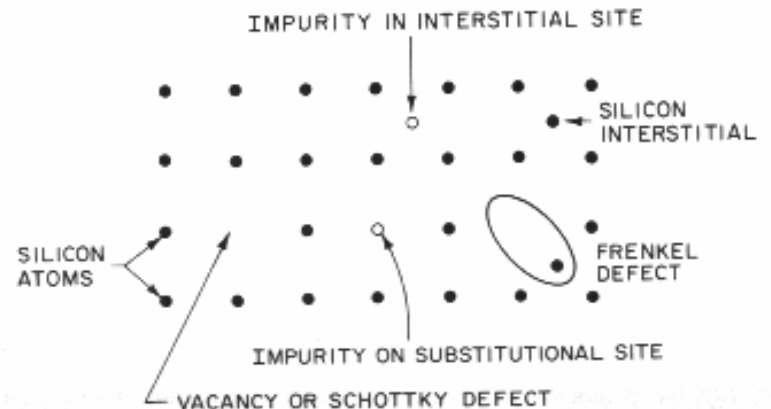
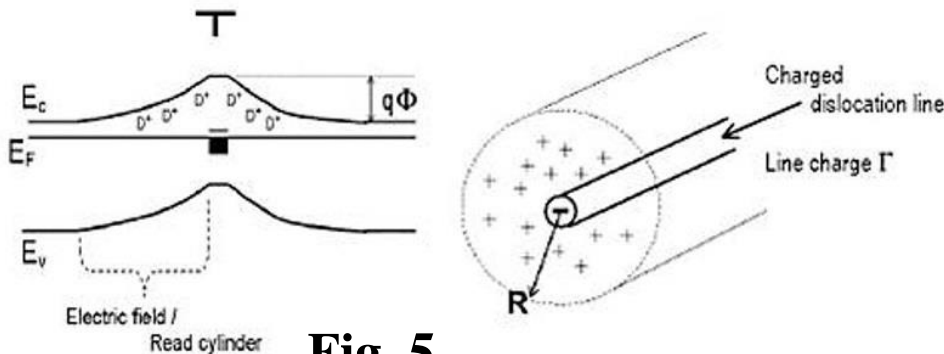
## 1.2. Changes in the rock conductivity under influence of tectonic strain 7

Pioneering investigations of strain-induced polarization and depolarization in a solid dielectric were provided by Stepanow (1933) who observed the appearance of an electric potential difference between opposite sides of an ionic crystal under slow strain. This effect cannot be explained solely by pyro-electricity or piezoelectricity because it was observed in quite different materials. Caffin and Goodfellow (1955) and Fishbach and Nowick (1958) have shown that this phenomenon in ionic crystals can result from the motion of charged dislocations under mechanical stress.

### Dislocation mechanism of rock conductivity



$J = q_d \dot{\epsilon} / b$  – density of dislocation current;  
 $q_d = 10^{-11}$  Кл/м – charge per unit dislocation length;  
 $\dot{\epsilon} = 10^4$  с<sup>-1</sup> – strain velocity;  
 $b = 0.5$  нм – absolute value of Burgers vector.



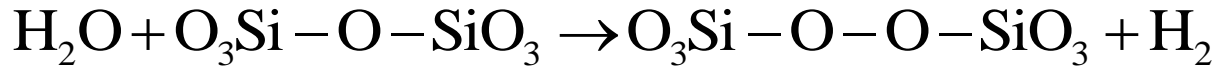
$$\delta B \approx \frac{\mu_0 JV}{4\pi r^2}, \quad E \approx \frac{JV}{4\pi\sigma r^3}$$

$V = 10^3 \text{ km}^3$  is volume of earthquake focus,  
 $r = 50 \text{ km}$  is distance to the earthquake epicenter,  
 $\sigma = 10^{-3} \text{ S/m}$  is mean conductivity of rocks

$$\Rightarrow \boxed{\delta B_{\text{max}} \approx 40 \text{ pT} \quad E_{\text{max}} \approx 0.6 \text{ }\mu\text{V/m}}$$

## Hypothesis of “positive holes” as highly mobile charge carriers

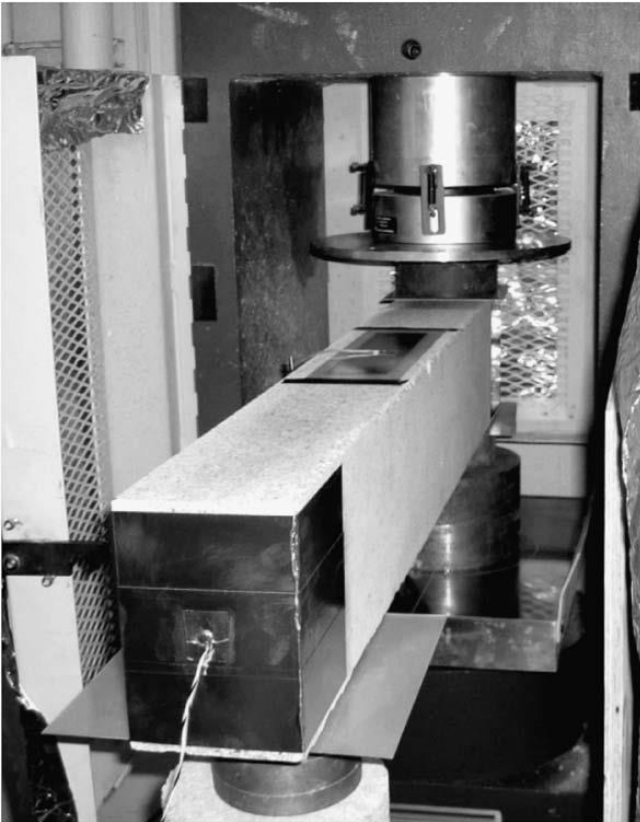
When traces of H<sub>2</sub>O structurally dissolve in the matrix of such silicates, the following reactions can take place



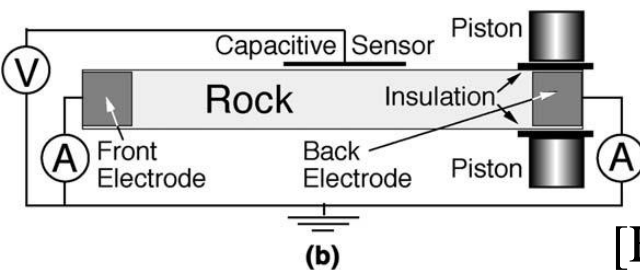
thereby producing the so-called peroxy bond. If the applied shear stresses exceed the elastic limit that results in the generation of large amount of dislocations, the peroxy link can be destroyed due to intersection of the mobile dislocation and the peroxy link. When the broken peroxy link meets O<sup>2-</sup>, it acts as an electron receptor, which can hold the electron for a long time. The O<sup>2-</sup>, which has donated the electron, turns into O<sup>-</sup>. This new anion plays a role of positive hole because it has one electron less as compared to all other oxygen anions.



[e.g., Freund, 2002; Tzanis and Vallianatos, 2002; Freund and Pilorz; 2012]



(a)



(b)

$$5 \cdot 10^3 \text{ A/km}^3 \times V$$

$$V = 1.8 \cdot 10^{-11} \text{ km}^3$$

$$I = 90 \text{ nA}$$

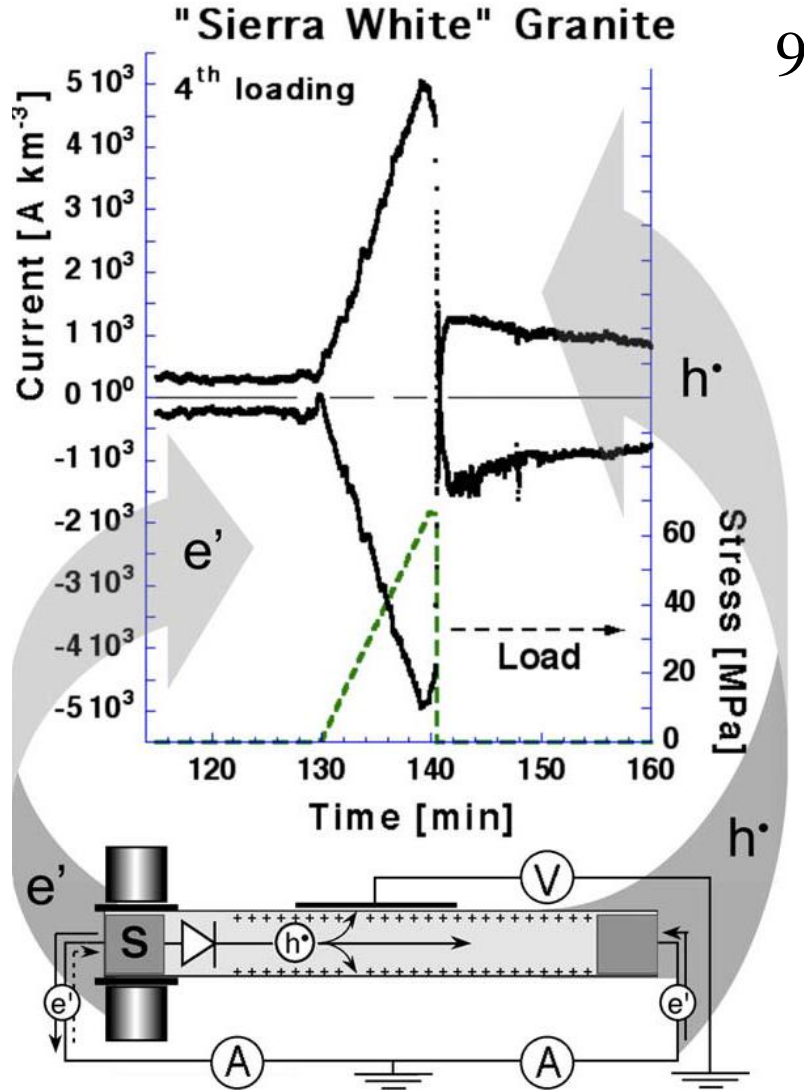
$$j = 6 \text{ } \mu\text{A/m}^2$$

$$I = jS_{earth}$$

$$S_{earth} = 10^2 \text{ km}^2$$

$$I = 600 \text{ A}$$

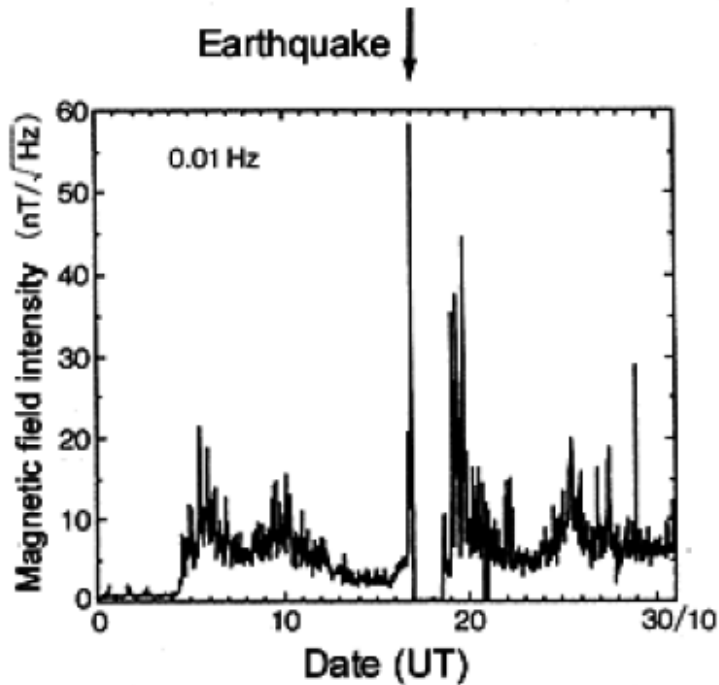
**Fig. 7.**  
[Freund, Takeuchi and Bobby, 2006]



**Fig. 2.** Two currents flowing out of the stressed rock volume, the "source" S, and a schematic representation of the current flow through the external circuit and inside the rock passing through the interface between stressed/unstressed rock which acts as a barrier for electrons.

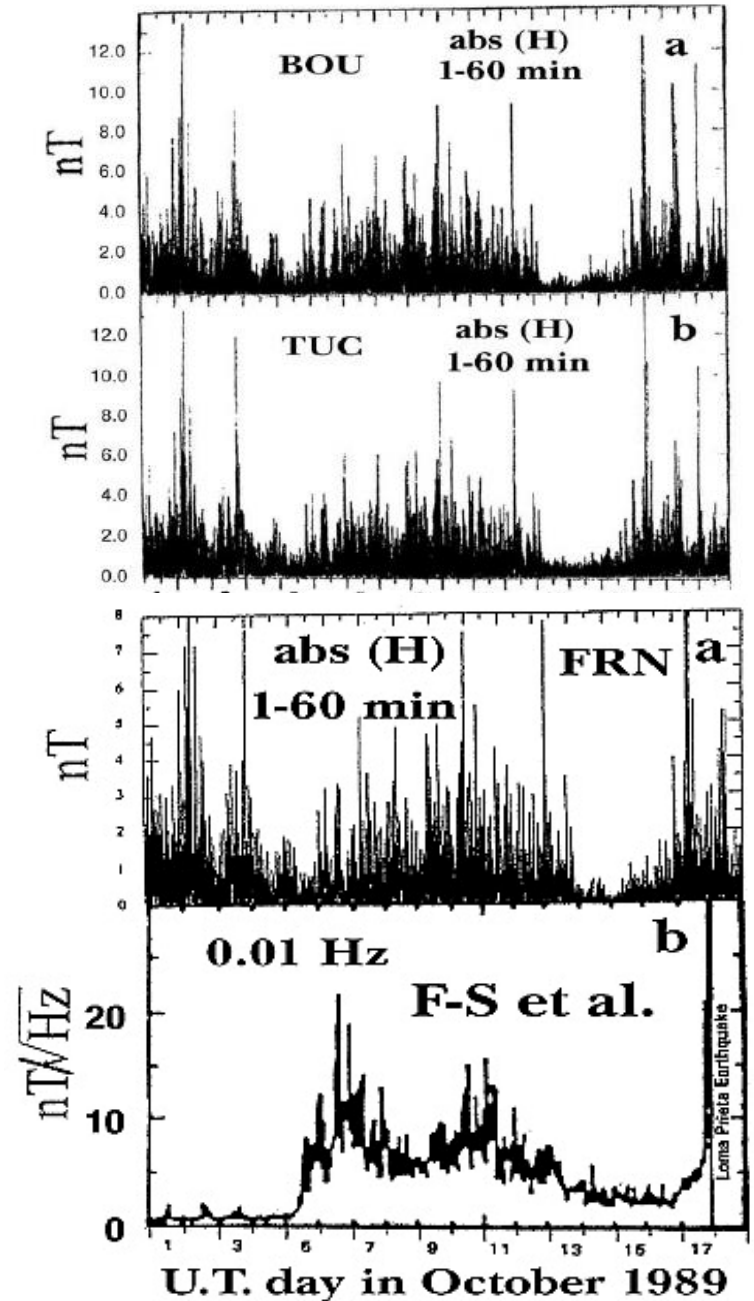
**Fig. 1.** (a) Granite slab placed in the press, ready for the uniaxial compression tests. The granite slab (1.2 m long, 10 · 15 cm<sup>2</sup> cross section) is fitted with two Cu electrodes (each 30 · 15 cm<sup>2</sup>), one at the back end and one at the front end, plus a non-contact capacitive sensor for measuring the surface potential. The rock is insulated from the pistons and the press by 0.8 mm thick polyethylene sheets (>10<sup>14</sup> Ω cm). (b) Block diagram of the electric circuit for allowing the self-generated currents to flow out of the stressed rock volume.

## 2. Abnormal ULF electromagnetic noise possibly related to earthquakes <sup>10</sup>



**Fig. 8.** Geomagnetic field perturbations prior to earthquake in Loma Prieta (1989,  $M_s=7.1$ ). Taken from Fraser-Smith et al., 1990.

**Fig. 9.** Campbell, W.H. (2009). Natural magnetic disturbance fields, not precursors, preceding the Loma Prieta earthquake, *J. Geophys. Res.*, **114**, A05307, doi:10.1029/2008JA013932. →



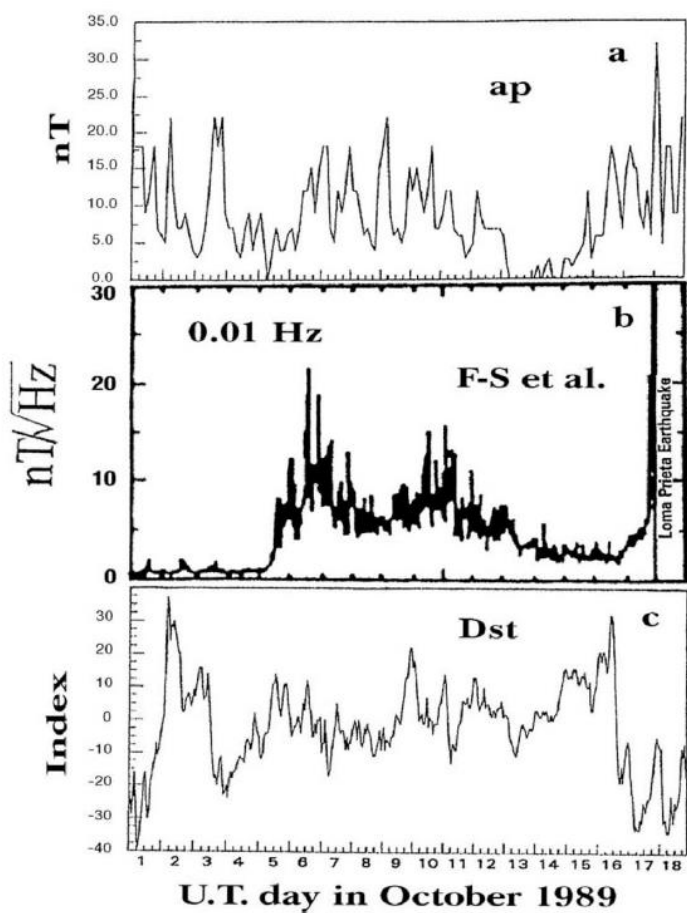


**Figure 3.** Campbell's [2009] Figure 1 comparing (a) the *ap* planetary magnetic index and (c) the *Dst* magnetic index with (b) data for the same 1–18 October 1989 time interval copied from Figure 3 of LP (reproduced as Figure 2 in this paper).

**Fig. 10.**

[Fraser-Smith et al., JGR, 2011]

**Fig. 11.** →

[Masci and Thomas, JGR, 2015]

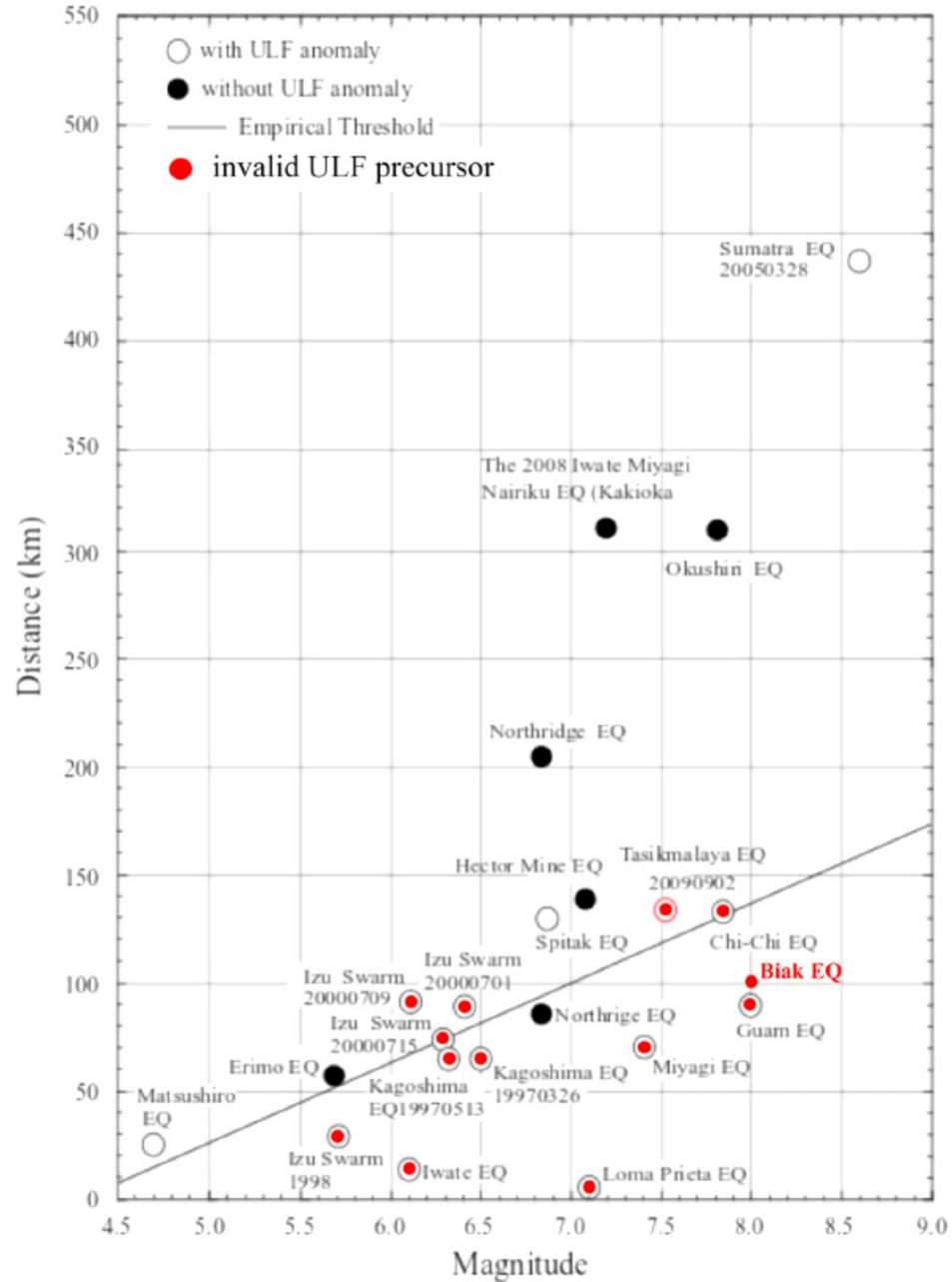


**Figure 1.** The empirical relationship proposed by Hattori et al. [2004] [see Febriani et al., 2014, Figure 10] between the earthquake magnitude and the distance from the epicenter of the ULF station where the preseismic anomaly was observed. The Biak earthquake has been included as reported in the original view of Hattori et al. [2004]. Note that the relationship was derived mainly using invalid ULF precursors (see Table S1 in the supporting information).

## Two source mechanisms for ULF electromagnetic field generation

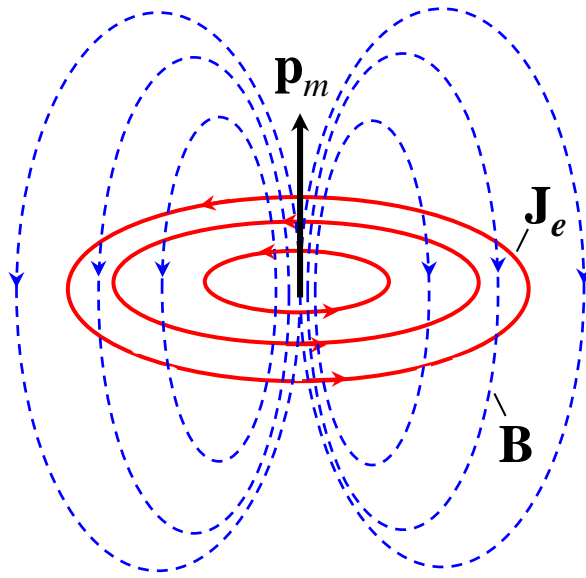


**Fig. 12.** Effective magnetic dipole  $\mathbf{p}_m$ . Closed extrinsic current  $\mathbf{J}_e$  generates poloidal magnetic field  $\mathbf{B}$ .

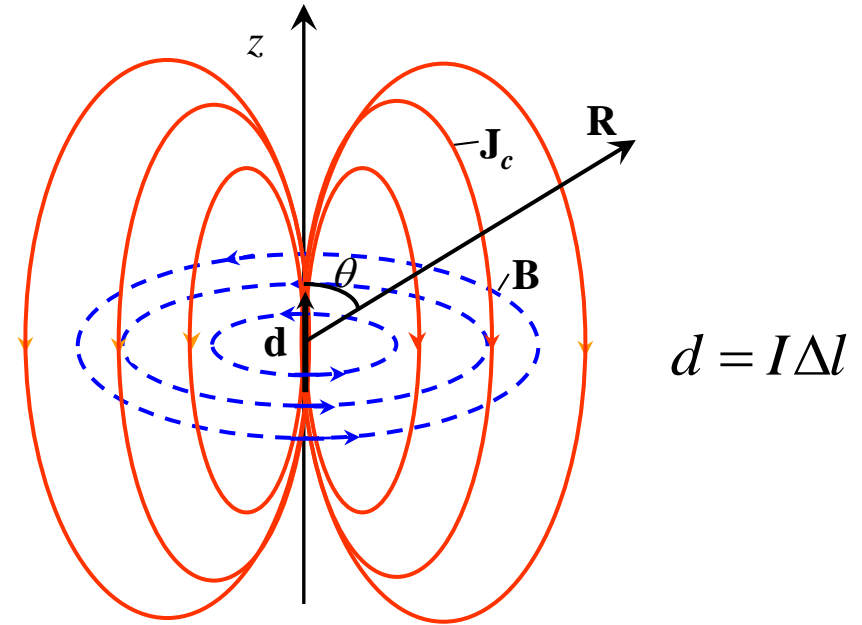


**Fig. 13.** Current element (electric dipole)  $d=I\Delta l$ . Extrinsic current  $I$  is closed through conduction current  $\mathbf{J}_c$  that results in generation of toroidal magnetic field  $\mathbf{B}$ .

$$B = \frac{\mu_0}{4\pi R^3} \left\{ \frac{3(\mathbf{R} \cdot \mathbf{p}_m) \mathbf{R}}{R^2} - \mathbf{p}_m \right\}. \quad (1) \quad \mathbf{E} = \frac{1}{4\pi\sigma R^3} \left\{ \frac{3(\mathbf{R} \cdot \mathbf{d}) \mathbf{R}}{R^2} - \mathbf{d} \right\}, \quad B_\varphi = \frac{\mu_0 d \sin \theta}{4\pi R^2}$$

**Rough estimate of the frequency of electromagnetic perturbations,  
the source of which is located near the focus of the earthquake**

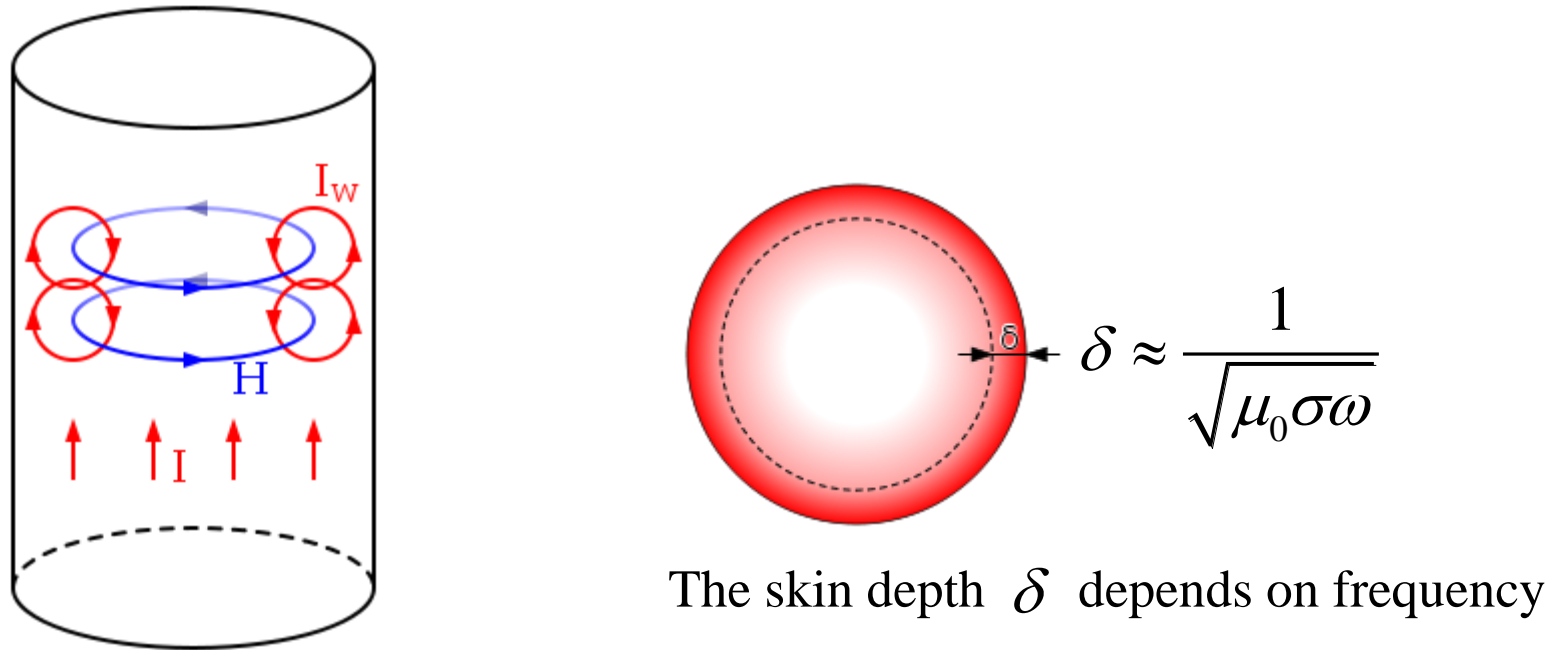


**Fig. 14.** Illustration of the skin effect.

$$\sigma = 10^{-3} \text{ S/m}, \quad \delta = 30 \text{ km.}$$

$$\omega \approx \frac{1}{\mu_0 \sigma \delta^2} \approx \frac{1}{4\pi \cdot 10^{-7} \cdot 10^{-3} \cdot (3 \cdot 10^4)^2} \approx 1 \text{ Hz}$$

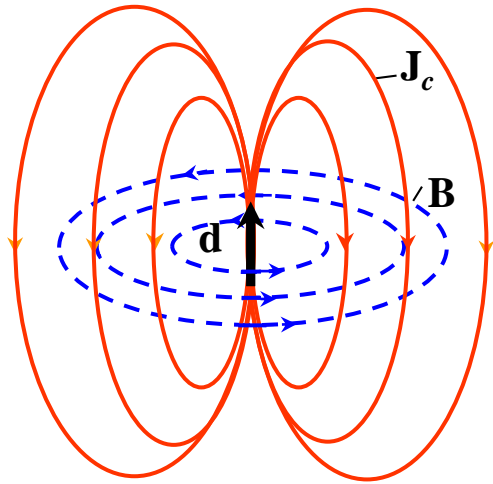


**Fig. 15.** In the model of Molchanov and Hayakawa (1994, 1995), each microcrack is assumed to be equivalent to an electric dipole.

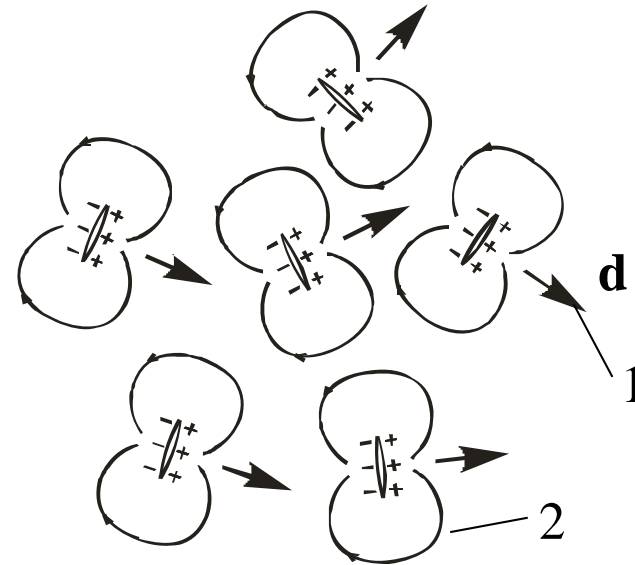


**Fig. 16.** The vectors  $\mathbf{d}$  of dipole moments (current elements) of all the cracks are co-directed. 1 – vectors of dipole moments; 2 – lines of electric micro-currents.

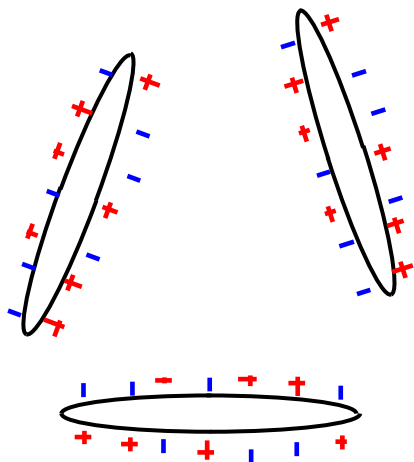


**Fig. 17.** Actually, the charges on the crack sides form a fluctuation mosaic. Due to the incoherent nature of real "emitters", the estimate by Molchanov and Hayakawa (1994, 1995) should be reduced by  $N^{1/2}$  times, where  $N$  is the number of microcracks ( $N \gg 1$ ).

## 2.2. Perturbations of geomagnetic field caused by acoustic emission of cracks situated in conducting rocks 15

The acoustic emission of cracks causes the motion of the conducting medium, which in turn results in the generation of electric currents due to the induction effect in the geomagnetic field  $\mathbf{B}_0$ . This leads to the generation of geomagnetic perturbations  $\mathbf{B}$ .

### Basic equations

$$\nabla \times \mathbf{B} = \mu_0 \sigma (\mathbf{E} + \mathbf{V} \times \mathbf{B}_0) ,$$

$$\nabla \times \mathbf{E} = -\partial \mathbf{B} / \partial t .$$

The current density resulted from the motion of conducting medium is  $\mathbf{j}_{\text{ext}} = \sigma (\mathbf{V} \times \mathbf{B}_0)$ , while  $\mathbf{j}_c = \sigma \mathbf{E}$  stands for conduction current

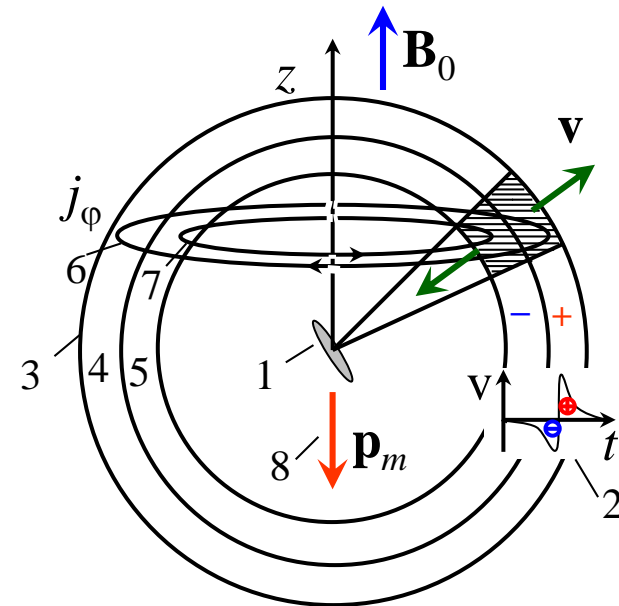


**Fig. 18.** Perturbations of the Earth's magnetic field. (1) tensile crack, (2) profile of the seismic wave, (3) wave front, (4) the compression region, (5) the rarefaction region, (6) and (7) the azimuthal electric current  $j_\phi$  caused by the movement of the rock, (8) the effective magnetic moment  $\mathbf{p}_m$  of the current system. **The effective magnetic moments  $\mathbf{p}_m$  are co-directed regardless of the orientation of the cracks, which creates the effect of coherent amplification of the ULF perturbations [Surkov, 1997].**

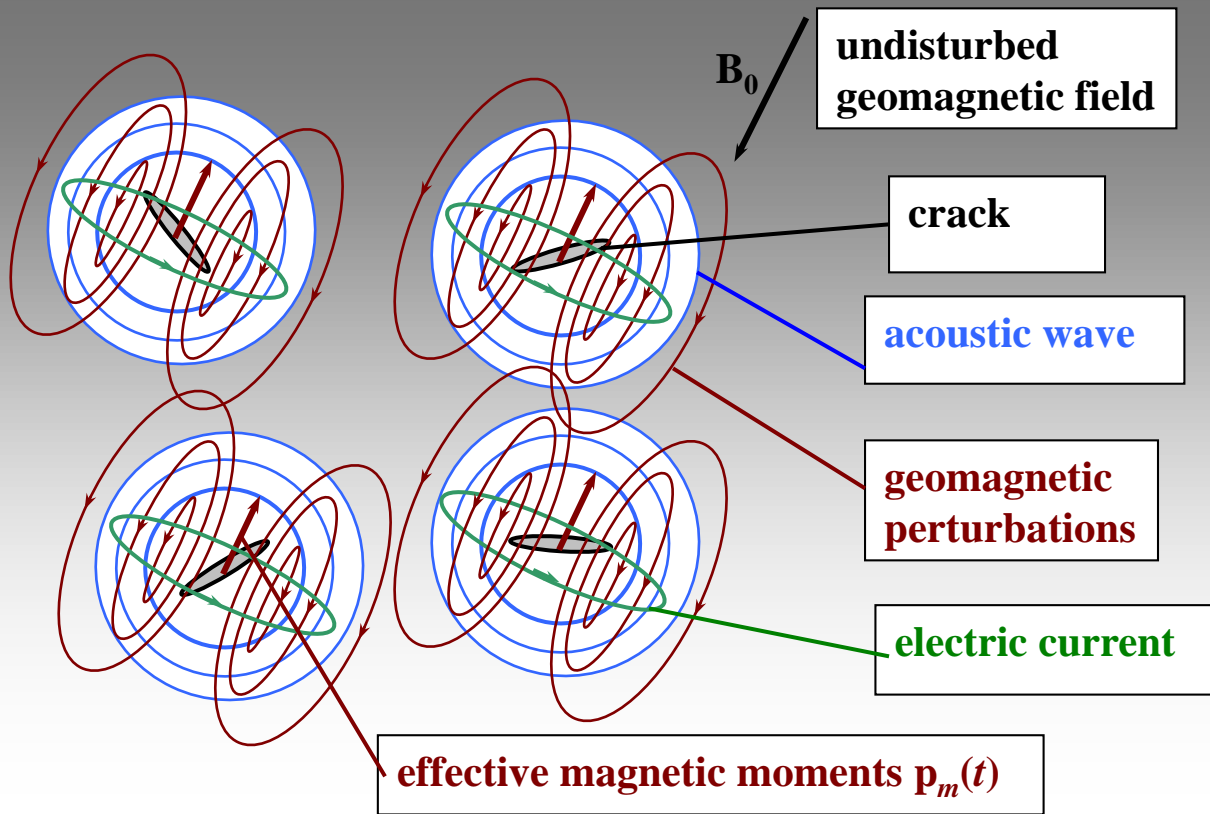


**Fig. 19.** Illustration of coherent ULF effect

Estimate of the amplitude of ULF electromagnetic noise produced by an ensemble of growing cracks [Surkov, 1997; Surkov and Hayakawa, 2006]

$$\delta B \sim \frac{\mu_0 \sigma C_t V B_0}{4\pi C_l r} \frac{d\langle p \rangle}{dt},$$

where  $d\langle p \rangle/dt \sim \Delta p/\Delta t$  is derivative of the average porosity of the medium,  $V$  is the volume of fracture zone,

$r$  is distance from the earthquake focus,  $\sigma$  is conductivity of the medium,  $C_l$  and  $C_t$  are velocities of longitudinal and transverse seismic waves (p- and s-waves), respectively.

$$\Delta p \sim 0.1-0.01, \quad \Delta t \sim 10^3 - 10^4 \text{ s}, \quad L \approx 64 \cdot 10^3 \text{ km} (M = 7), \quad r = 70 \text{ km},$$

$$C_t = 0.5C_l, \quad B_0 = 5 \cdot 10^{-5} \text{ T}, \quad \sigma = 10^{-3} \text{ S/m}$$

$$\Rightarrow \boxed{\delta B \sim 2 - 2 \cdot 10^2 \text{ pT}}$$

## 2.3. Electrokinetic effect in porous water-saturated rocks

**Fig. 20.** Model of a surface diffusion layer near the wall of a channel filled with underground water.

1 – Stern layer consisting of two sublayers;  
 2 – the region of mobile ions  
 3 – adsorbed ion;  
 4 – hydrated ion.

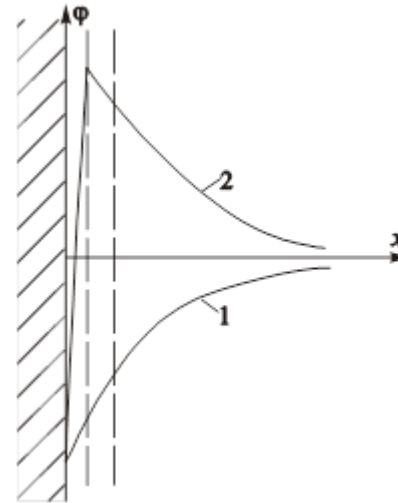
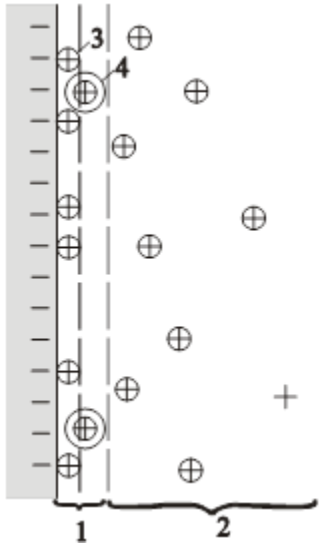


**Fig. 21.** Approximate dependence of the electric potential on the distance near the channel wall.

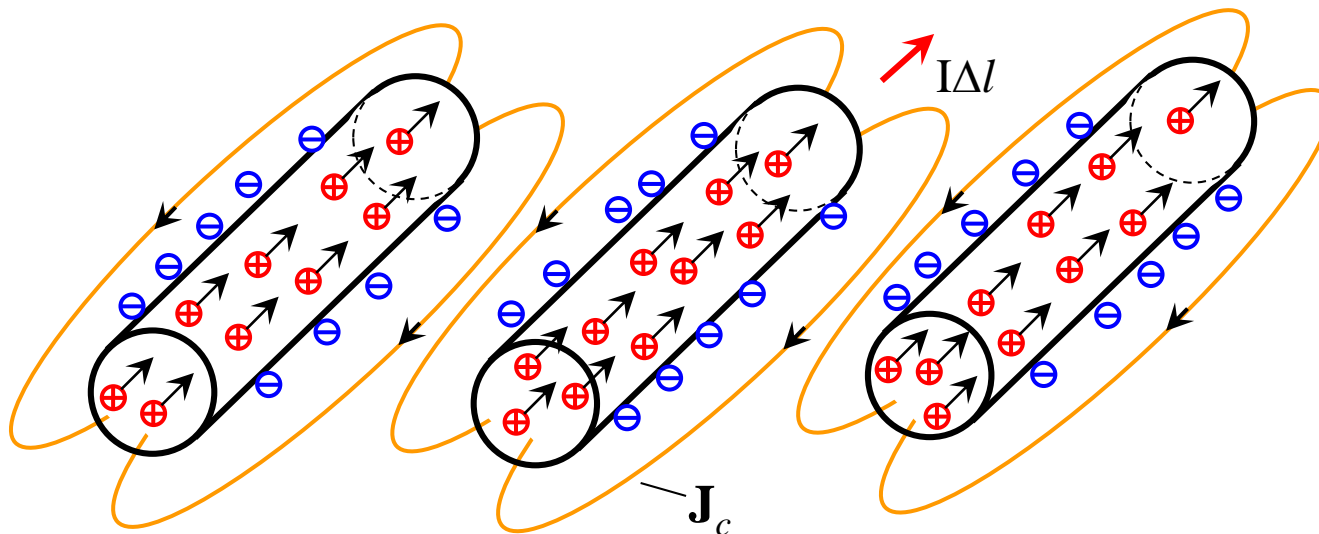


**Fig. 22.** Model of electrokinetic current in underground channels (cracks) filled with fluid. The electrokinetic current is closed by the conduction current  $\mathbf{J}_c$  shown with the yellow lines.

The density of the electrokinetic current averaged over the cross-section of the medium:

$$\mathbf{j}_e = -\sigma C_{\text{EK}} \nabla P, \quad C_{\text{EK}} \sim \frac{\varepsilon \varepsilon_0 \zeta n}{\eta \sigma} \approx 10^{-6} - 10^{-8} \text{ V/Pa}$$

$\sigma$  is mean rock conductivity,  $C_{\text{EK}}$  is streaming potential coefficient,  $\nabla P$  is gradient of groundwater in pore space,  $\varepsilon$  and  $\eta$  are dielectric permittivity and viscosity of underground fluid,  $\varepsilon_0$  is dielectric constant,  $\zeta$  is contact potential difference between pore wall and fluid,  $n$  is the medium porosity.

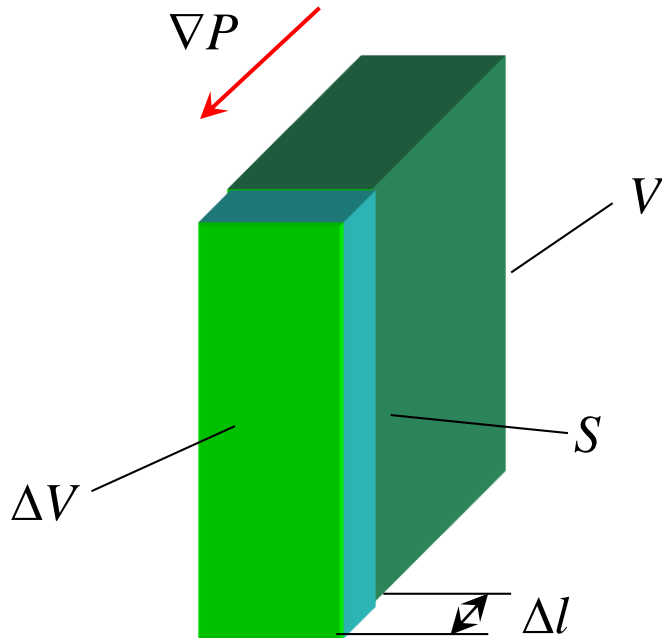


**Fig. 23.** A model of sealed underground compartments  $V$  with high pore pressure  $P$ . The fluid filtration through the surface  $S$  towards the low pressure region  $\Delta V$  may be triggered by weak seismic events to generate electrokinetic effects [Bernard, 1992; Fenoglio et al., 1995].

Estimate of the geomagnetic perturbations in the framework of this model:

$$d = I \Delta l \approx j_e \Delta V = \sigma C_{\text{EK}} |\nabla P| \Delta V$$

$$r = 10 \text{ km}, \quad \Delta V = 10^3 - 10^5 \text{ m}^3, \quad \Rightarrow \quad \delta B_{\text{max}} \sim \frac{\mu_0 \sigma \Delta C_{\text{EK}} |\nabla P| \Delta V}{4\pi r^2} \approx 10^{-2} \text{ pT}$$

## Theoretical models explaining the generation of ULF electromagnetic field variations in rocks

- **Variations of rock conductivity** [e.g., Myachkin et al., 1972; Sobolev et al., 1972; Rikitake and Yamazaki 1978, 1985; Honkura, 1981; Rikitake, 1987; Sheng and Chen, 1988; Freund 2000; Freund and Pilorz; 2012 ]
- **Electrokinetic effects in water-saturated rocks** [Bernard, 1992; Fenoglio et al., 1995; Surkov et al., 2002]
- **Perturbations of the geomagnetic field resulted from acoustic emission of cracks in conductive ground** [Surkov, 1997; Surkov and Hayakawa, 2006]
- **Rock electrization due to microfracturing** [Molchanov and Hayakawa, 1994, 1995].
- **Tectonomagnetic/piezomagnetic effect under deformation of magnetite rock** [e.g., Gershenzon et al., 1993],
- **Magneto-hydrodynamic effect caused by filtration of underground fluid** [e.g., Draganov et al, 1991],
- **Piezoelectric effect in quartz inclusions** [e.g., Cutolo, 1988; Kingsley, 1989]
- **Electric effect due to rock heating and evaporation of underground fluid in the vicinity of fault zone** [e.g., Lockner and Byerlee, 1985]
- **and etc.**

The above analysis of different mechanisms of the seismic-induced electromagnetic noise has shown that the amplitude of magnetic variation can be of the order of  $1\text{--}10\text{ pT/Hz}^{1/2}$  at epicentral distances smaller than  $50\text{--}100\text{ km}$  and this variation becomes practically undetectable at the distances greater than  $50\text{--}100\text{ km}$ .



### 3. Co-seismic electromagnetic phenomena

To all appearance Ivanov [1939, 1940] was the first who detected electromagnetic effect associated with the propagation of seismic waves in the ground. The potential difference between the buried electrodes was recorded at distances up to 120 m from the explosion site in the soil (the mass of the explosive charge is about 1.5 kg). This phenomenon called the seismoelectric effect of the second kind can be explained by the electrokinetic effect in fluid-filled cracks and channels contained in the surface layer of the ground [Frenkel, 1944].

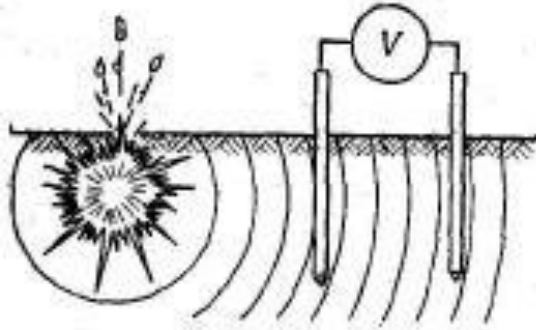


**Fig. 24.** The electrodes arrangement to detect seismoelectric effect of the second kind.

#### Two mechanisms of co-seismic phenomena

$$\nabla \times \mathbf{B} = \mu_0 \sigma (\mathbf{E} - C_{\text{EK}} \nabla P_f + \mathbf{V} \times \mathbf{B}_0).$$

Here  $\mathbf{B}$  and  $\mathbf{E}$  are perturbations of the Earth's magnetic and electric fields,  $\sigma$  is the ground conductivity,  $C_{\text{EK}}$  is streaming potential coefficient,  $\nabla P_f$  is gradient of pore fluid pressure,  $\mathbf{V}$  is mass velocity of the medium;  $\mathbf{B}_0$  is undisturbed geomagnetic field.

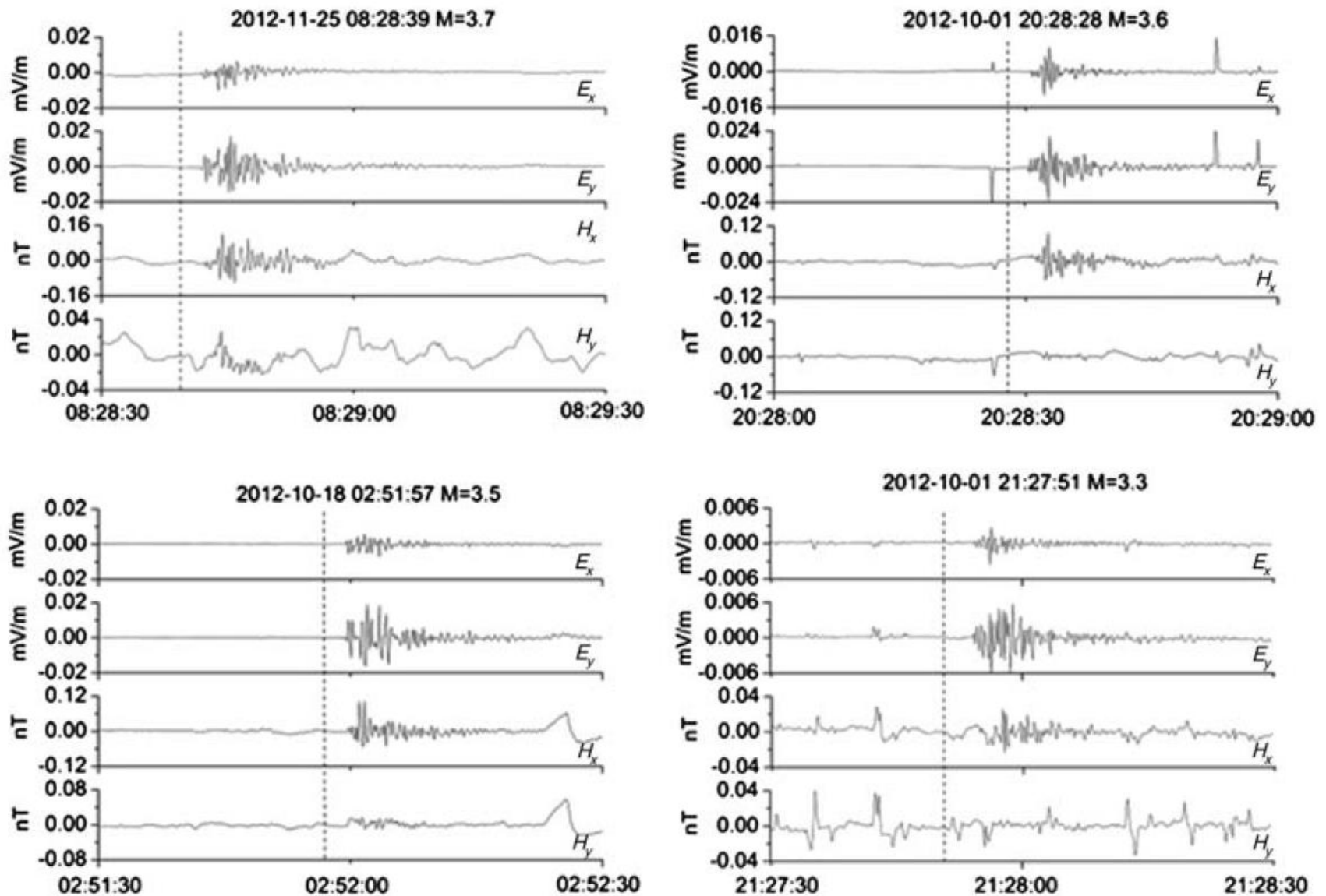


**Fig. 25.** Examples of electric ( $E_x - E_y$ ) and magnetic signals ( $H_x - H_y$ ) recorded between October and November 2012 at the CAMP MT station related to events with different magnitudes. The dashed lines indicate the origin time of the earthquakes.

[Balasco et al., 2014]

#### Basic equations

$$\mathbf{j} = \sigma(\mathbf{E} - C_{EK} \nabla P_f), \quad \mathbf{E} = -\nabla \varphi, \quad \nabla \cdot \mathbf{j} = 0.$$

$\mathbf{j}$  is electric current density,

$\mathbf{E}$  is strength of electric field,

$\sigma$  is conductivity of ground,

$C_{EK}$  is streaming potential coefficient,

$\nabla P_f$  is pressure gradient of groundwater

If  $\sigma$  and  $C_{EK}$  are approximately constant, then

$$\nabla^2 (\varphi - C_{EK} P_f) = 0 \quad \Rightarrow \quad \varphi - C_{EK} P_f = 0 \quad \boxed{\varphi = C_{EK} P_f}$$

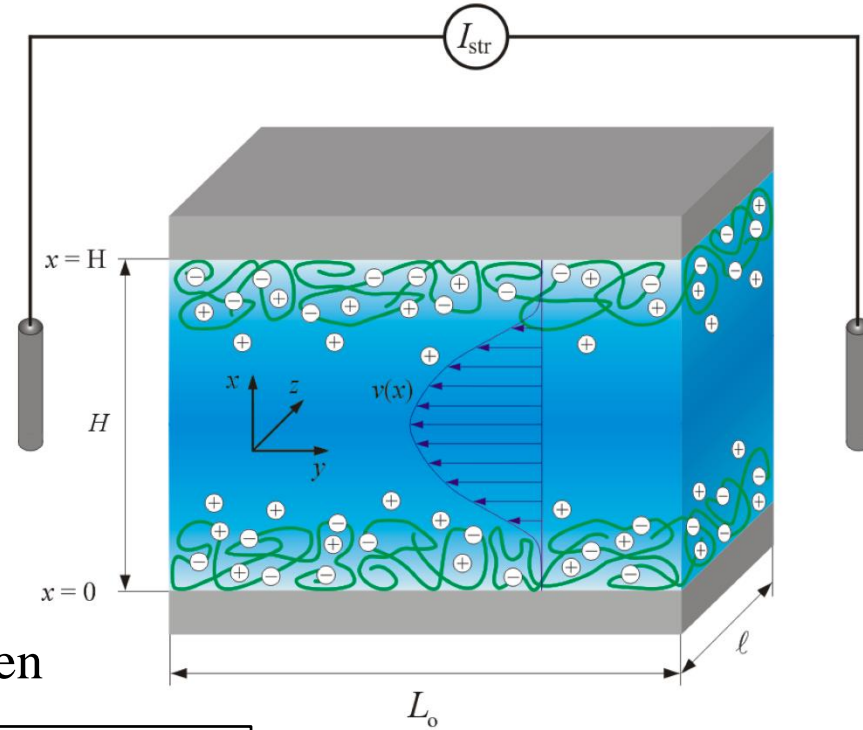


**Fig. 26.**

#### Theory of porous medium by Frenkel and Biot

$$\frac{1}{K_f} \frac{\partial^2 P_f}{\partial t^2} + \frac{(\beta - 1)}{\alpha} \frac{\partial^2 u_v}{\partial t^2} = \frac{1}{\alpha \rho} \nabla^2 P_f - \frac{\eta}{\rho k_p} \left( \frac{1}{K_f} \frac{\partial P_f}{\partial t} + \frac{\beta}{\alpha} \frac{\partial u_v}{\partial t} \right),$$

where  $u_v = \Delta V/V$  is volume strain,  $\alpha = 1 + (\beta - 1)K_f/K_s$ ,  $\beta = (1 - K/K_s)n^{-1}$

$$P_f = -\beta K_f \alpha^{-1} u_V, \quad \Rightarrow \quad \boxed{\varphi = C_{EK} P_f = -\beta K_f C_{EK} \alpha^{-1} u_V}$$

where  $u_V$  is volume strain

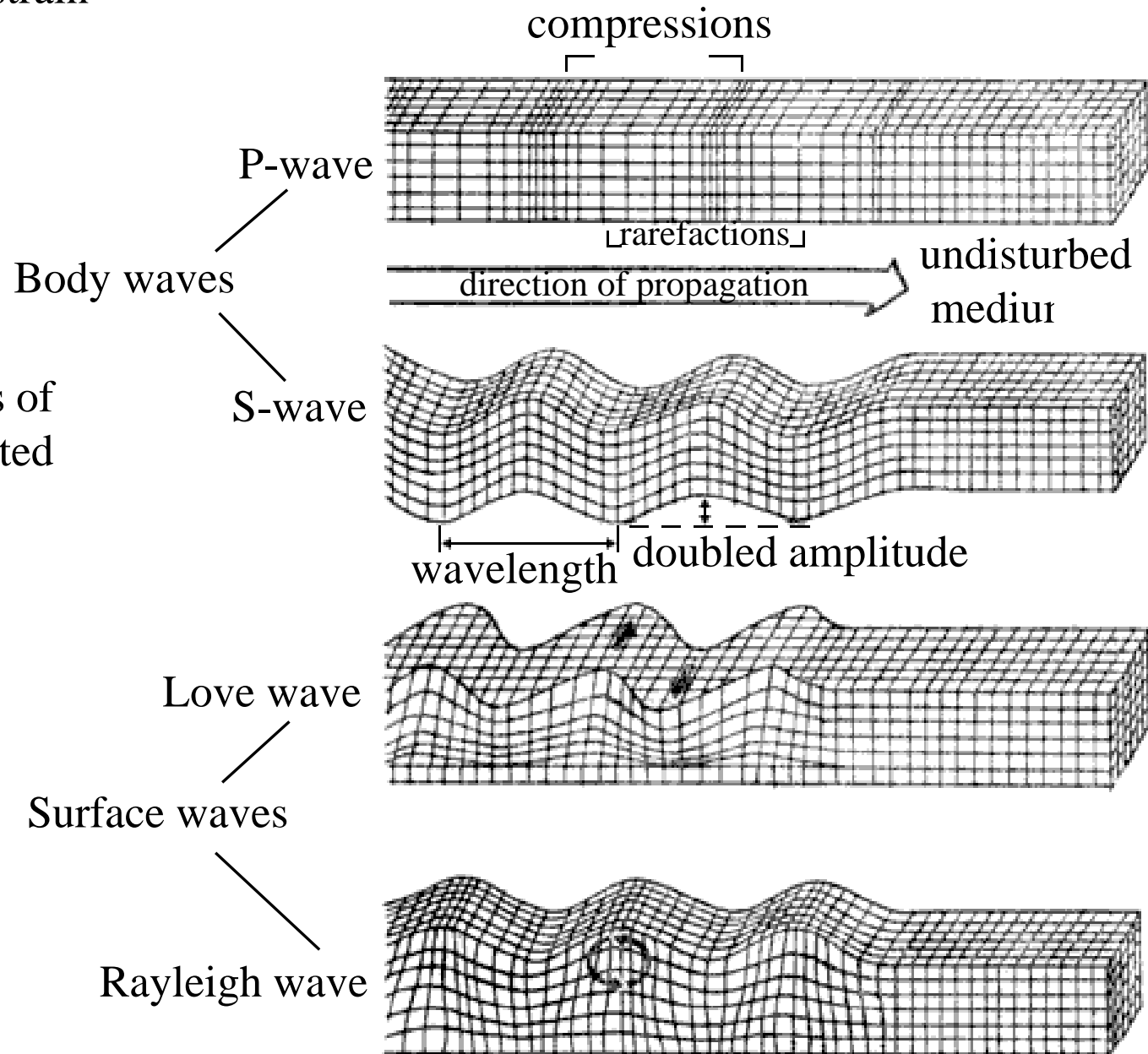


**Fig. 27.** Various types of seismic waves generated by earthquakes and volcano eruptions.

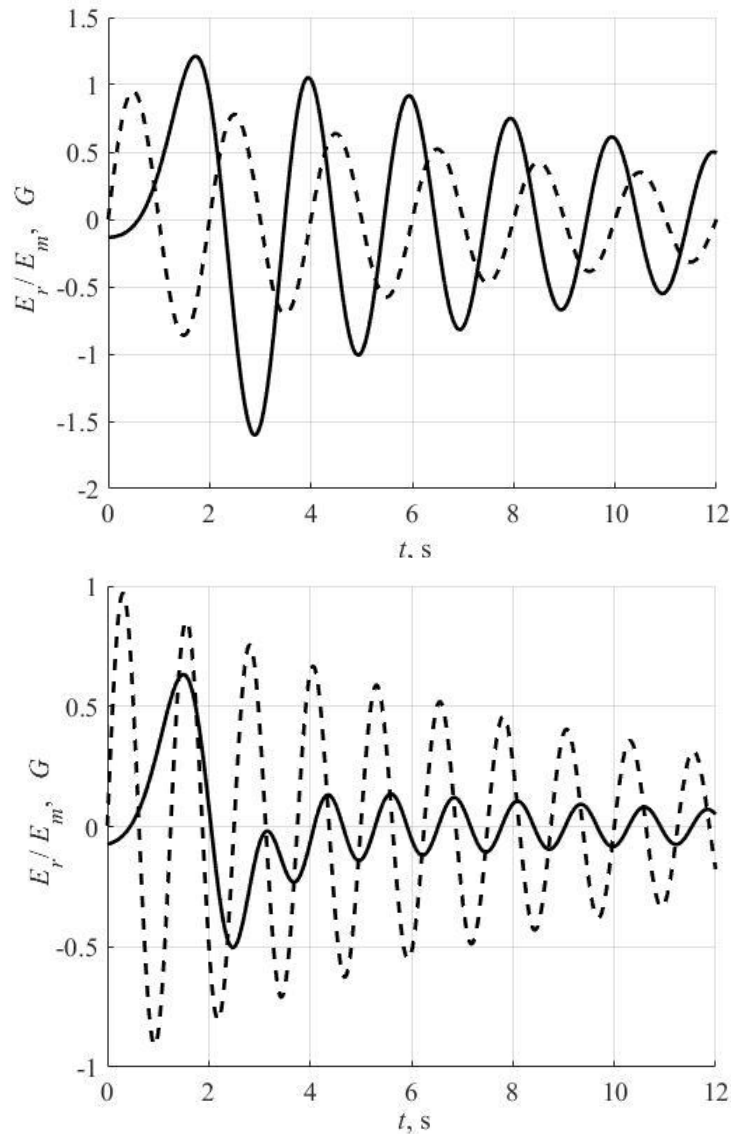


**Fig. 28.** Numerical modeling of co-seismic signal caused by quasi-oscillatory seismic wave; (a)  $f = 0.5$  Hz; (b)  $f = 0.8$  Hz [Surkov et al., 2018, 2020]

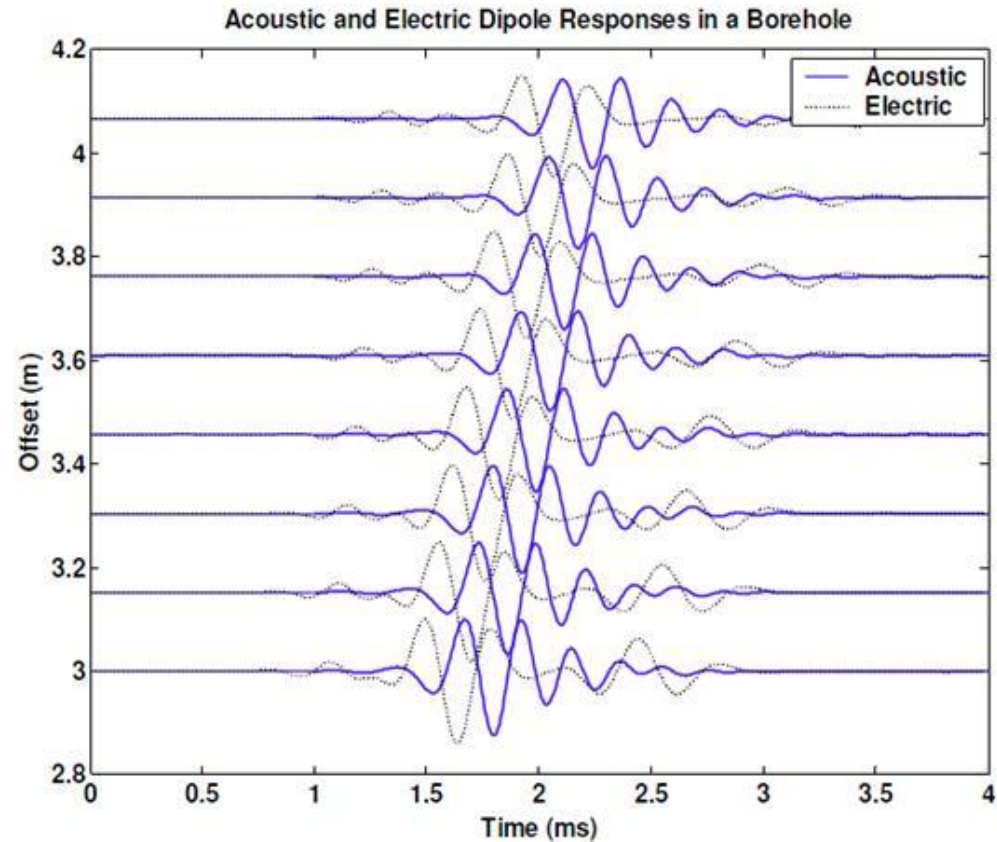


**Fig. 29.** Courtesy Zhu, Z. et al., Theoretical and Experimental Studies of Seismoelectric Conversions in Boreholes, Communications in Computational Physics, January, 2008

### 3.2. Geomagnetic field perturbations caused by seismic waves in conductive ground

Two regimes of propagation of geomagnetic field perturbations

$$\frac{\partial \mathbf{B}}{\partial t} = D \nabla^2 \mathbf{B} + \nabla \times (\mathbf{V} \times \mathbf{B}_0) \quad D = (\mu_0 \sigma)^{-1} \text{ is coefficient of magnetic diffusion}$$

$$\frac{\partial B}{\partial t} \sim \frac{B}{t} \quad D \nabla^2 B \sim D \frac{B}{r^2} \Rightarrow r_d^2 \sim Dt \quad \sigma = 10^{-3} \text{ S/m}, C_l = 5 \text{ km/s}$$

$$\sqrt{Dt} \sim C_l t \Rightarrow t_* \sim D/C_l^2 \approx 32 \text{ s}$$

$$r_* \sim C_l t_* \approx 160 \text{ km [Surkov, 1997]}$$

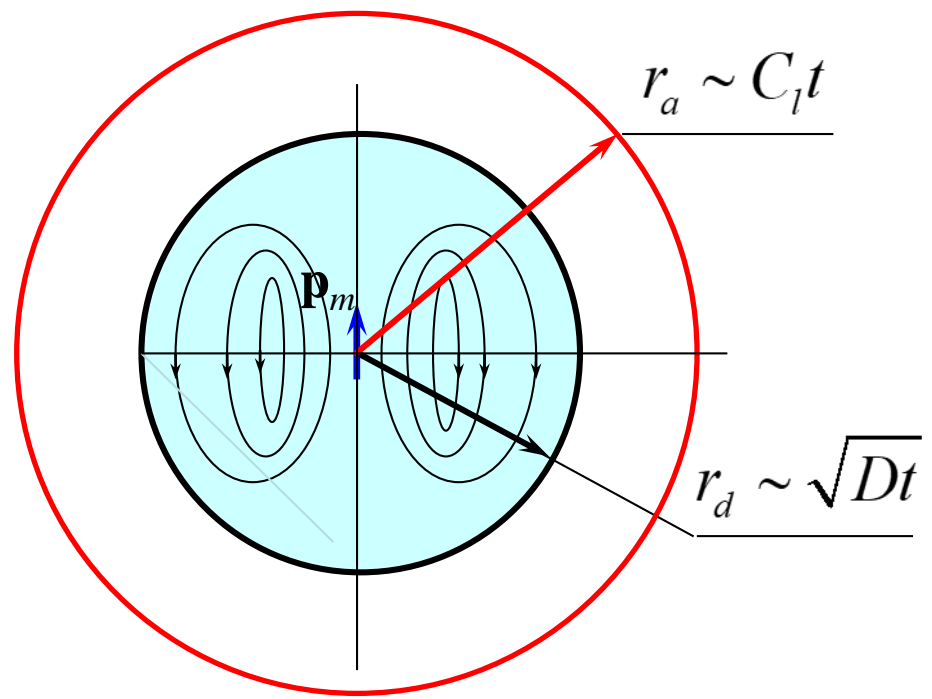
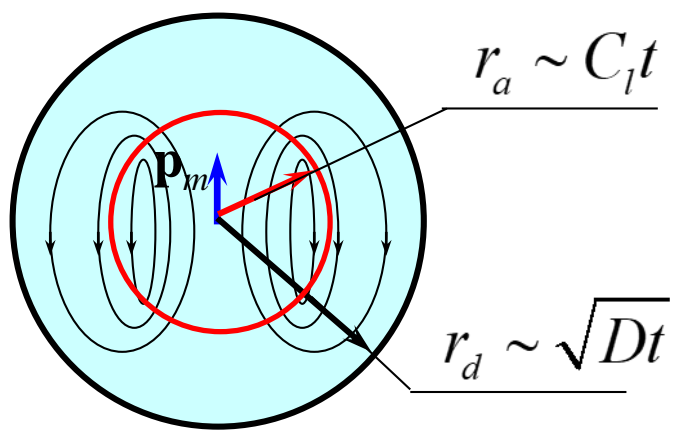


Fig. 30. Diffusion regime ( $t < t_*, r < r_*$ )

Fig. 31. Seismic regime ( $t > t_*, r > r_*$ )

**Estimate of magnitude of geomagnetic field perturbations  
caused by seismic wave propagation. Seismic regime**

$$\partial \mathbf{B} / \partial t = D \nabla^2 \mathbf{B} + \nabla \times (\mathbf{V} \times \mathbf{B}_0)$$

$$\frac{\partial B}{\partial t} \sim \frac{B}{T} \quad D \nabla^2 B \sim D \frac{B}{\lambda^2} \quad |\nabla \times (\mathbf{V} \times \mathbf{B}_0)| \sim \frac{V B_0}{\lambda}$$

Here  $T$  is wave period,  $\lambda$  is wavelength, and  $D$  is coefficient of magnetic diffusion

$$T \ll \frac{2\pi}{\mu_0 \sigma C_1^2} \approx 20 - 200 \text{ s} \quad \Rightarrow \quad D \frac{B}{\lambda^2} \sim \frac{V B_0}{\lambda} \quad \Rightarrow \quad B \sim \mu_0 \sigma \lambda V_{\max} B_0$$

$$M = 7, \quad r = 1000 \text{ km}, \quad \Rightarrow \quad B \approx 0.012 - 0.12 \text{ nT}$$

[Gorbachev and Surkov, 1987; Guglielmi, 1987; Surkov, 1997]

**Estimate of electric field in a reference frame fixed to observer**

$$\mathbf{B}' = \mathbf{B}, \quad \mathbf{E}' = \mathbf{E} + \mathbf{V} \times \mathbf{B}_0 \quad \nabla \times \mathbf{B}' = \mu_0 \sigma \mathbf{E}'$$

$$\Rightarrow E' \sim \frac{b'}{\mu_0 \sigma} \sim V_{\max} B_0 \approx 0.16 \text{ } \mu\text{V/m}$$

The theory predicts that electromagnetic forerunner has to propagate not far as several seconds ahead of seismic wave.

$$r_* \sim C_1 t_* \approx 160 \text{ km}$$

$$t_* \sim D/C_1^2 \approx 32 \text{ s}$$

$$t > t_*, \quad r > r_*$$

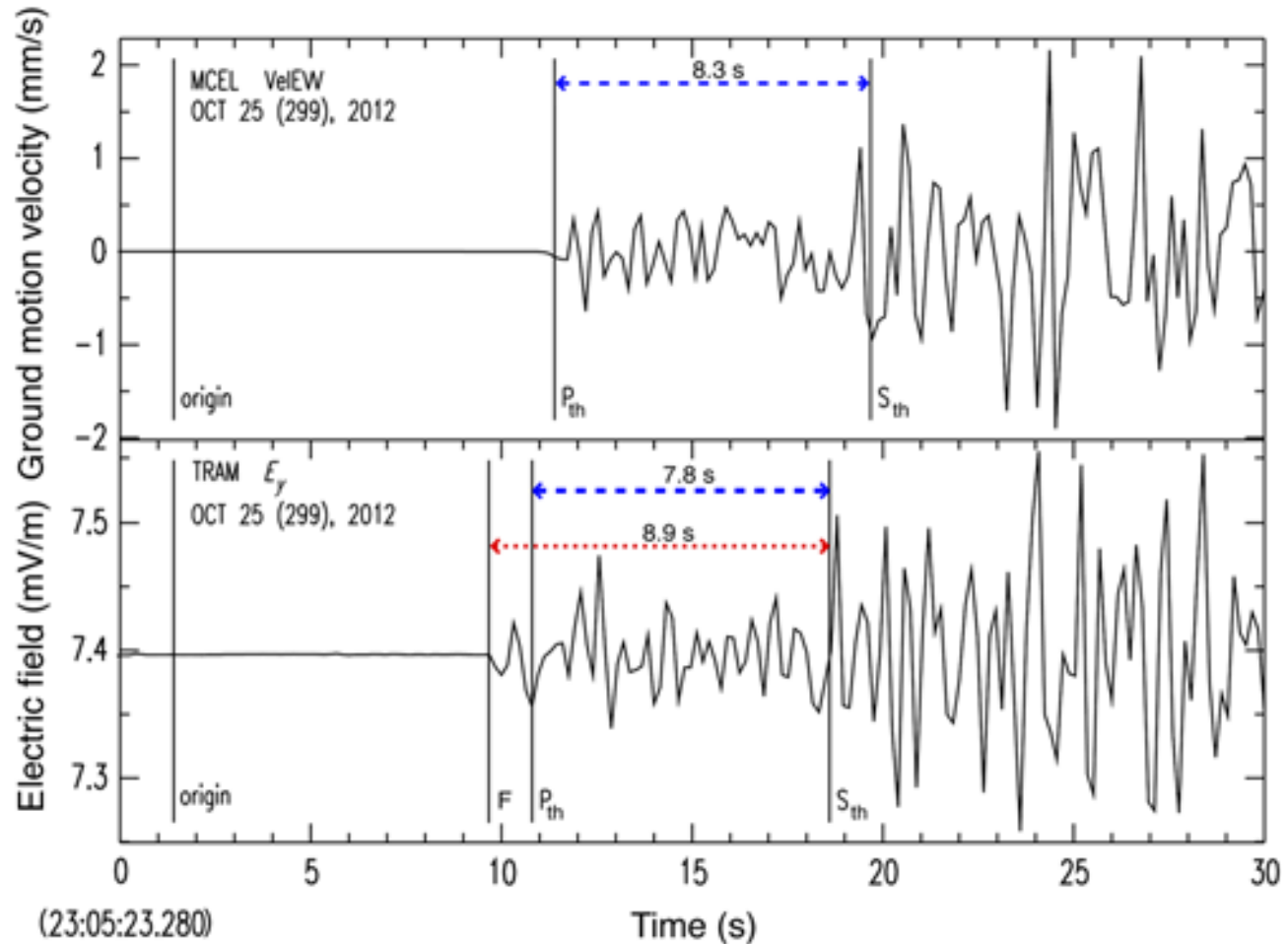


**Fig. 32.** Homologous components along the east–west direction of (top) the ground-motion velocity (mm/s) recorded at Monticello seismic station and (bottom) the electric field (mV/m) recorded at the TRAM station. Earthquake origin time (origin), theoretical P- and S-wave arrival times (P<sub>th</sub> and S<sub>th</sub>) at both stations, and the first motion (F pick) of the electric field are also reported. The dashed line indicates the S<sub>th</sub>–P<sub>th</sub> differential time at a station, whereas dotted line represents the S<sub>th</sub>–F differential time at the TRAM station [Balasco et al., 2014].

During the diffusion regime the amplitude of geomagnetic perturbations (GMPs) falls off more rapidly with distance due to the electromagnetic energy absorption and dissipation in conducting media. At a later moment the GMPs are localized in the vicinity of seismic wave front that results in a slow decrease of amplitude with distance. In this case the seismic and electromagnetic perturbations depend on distance in the same manner; that is, for the primary/longitudinal wave they decrease as  $r^{-1}$  whereas for the Rayleigh surface wave they vary as  $r^{-1/2}$ . The co-seismic GMPs caused by these large-scale tectonic phenomena may be detectable at large distances.

for bulk seismic waves  $\delta E, \delta B \sim \frac{1}{r}$

for surface seismic waves  $\delta E, \delta B \sim \frac{1}{r^{1/2}}$



### 3.3. Effect of acoustic-gravity waves on the ionosphere

Short acoustic waves caused by detonation on the ground surface

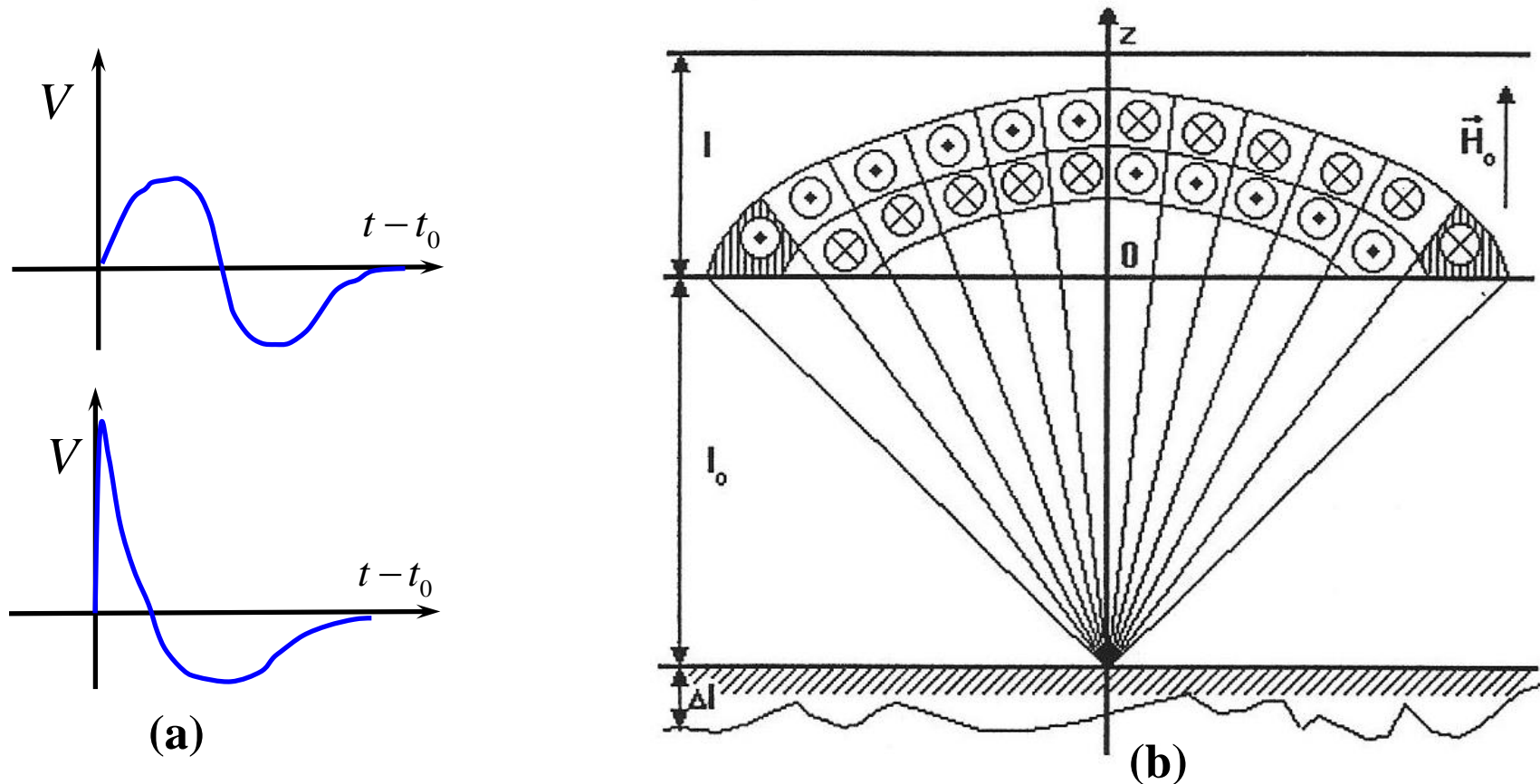


**Fig. 33.** (a) Typical curve for the gas velocity versus time for the "N-wave".  $t_0$  is the moment for wave to enter the point of space under consideration. (b) A model for the atmosphere ( $-l_0 < z < 0$ ) and ionospheric  $E$  layer ( $0 < z < l$ ), applied in the present paper. Shaded areas correspond to those of the acoustic wave generating uncompensated extrinsic currents.

## The parameter ranges at which the emission of acoustic (A) and internal gravity waves (IGW) in the atmosphere is possible

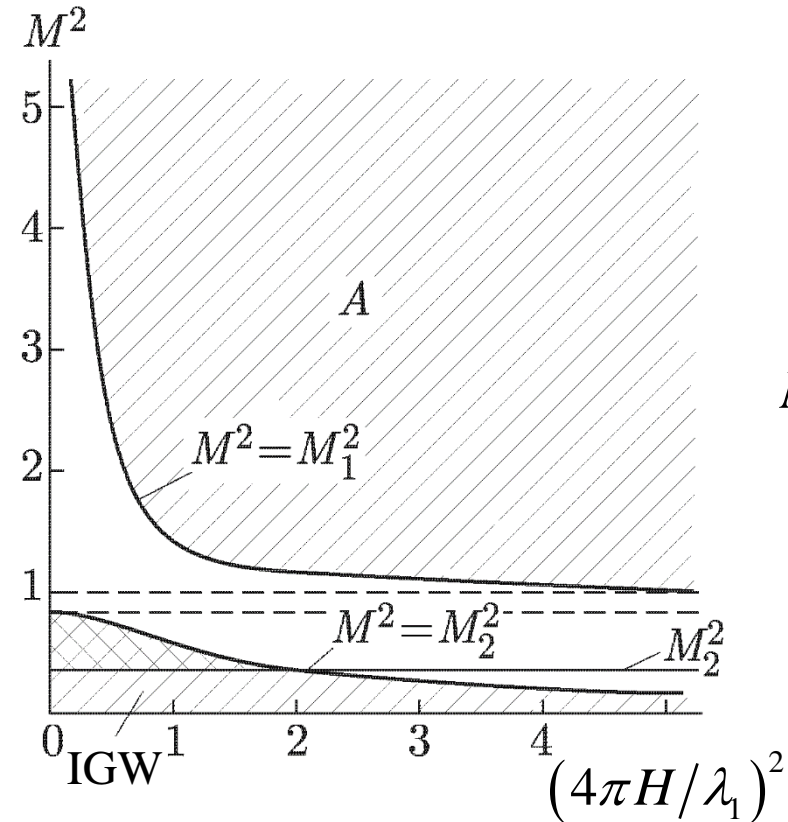


**Fig. 34.**

Surface displacement caused by the propagation of the Rayleigh wave :  $z = z_0 \exp\{ik_1(x - V_R t)\}$

$$k_1 = \frac{2\pi}{\lambda_1}, \quad \alpha = \frac{1}{2H}, \quad A^2 = 4\gamma^{-2}(\gamma - 1) < 1$$

$$M_{1,2}^2 = (2k_1^2)^{-1} \left[ (k_1^2 + \alpha^2) \pm \sqrt{(k_1^2 + \alpha^2)^2 - 4A^2\alpha^2k_1^2} \right]$$

$H$  is the height of homogeneous atmosphere,  
 $\gamma$  is adiabatic index,

$V_R$  is Rayleigh velocity,

$c$  is the speed of sound in the air,

$M = V_R / c$  is Mach number.

Consider, for example, the pressure waves recorded after the Alaskan earthquake. According to [Bolt, 1964], in Palisades (New York, USA), the maximum vertical displacement of the soil, equal to 42 mm, was observed for the first Rayleigh wave, which had a period of 23 s and propagated at a speed of 3 – 3.3 km/s. The maximum pressure amplitude was 4 Pa.

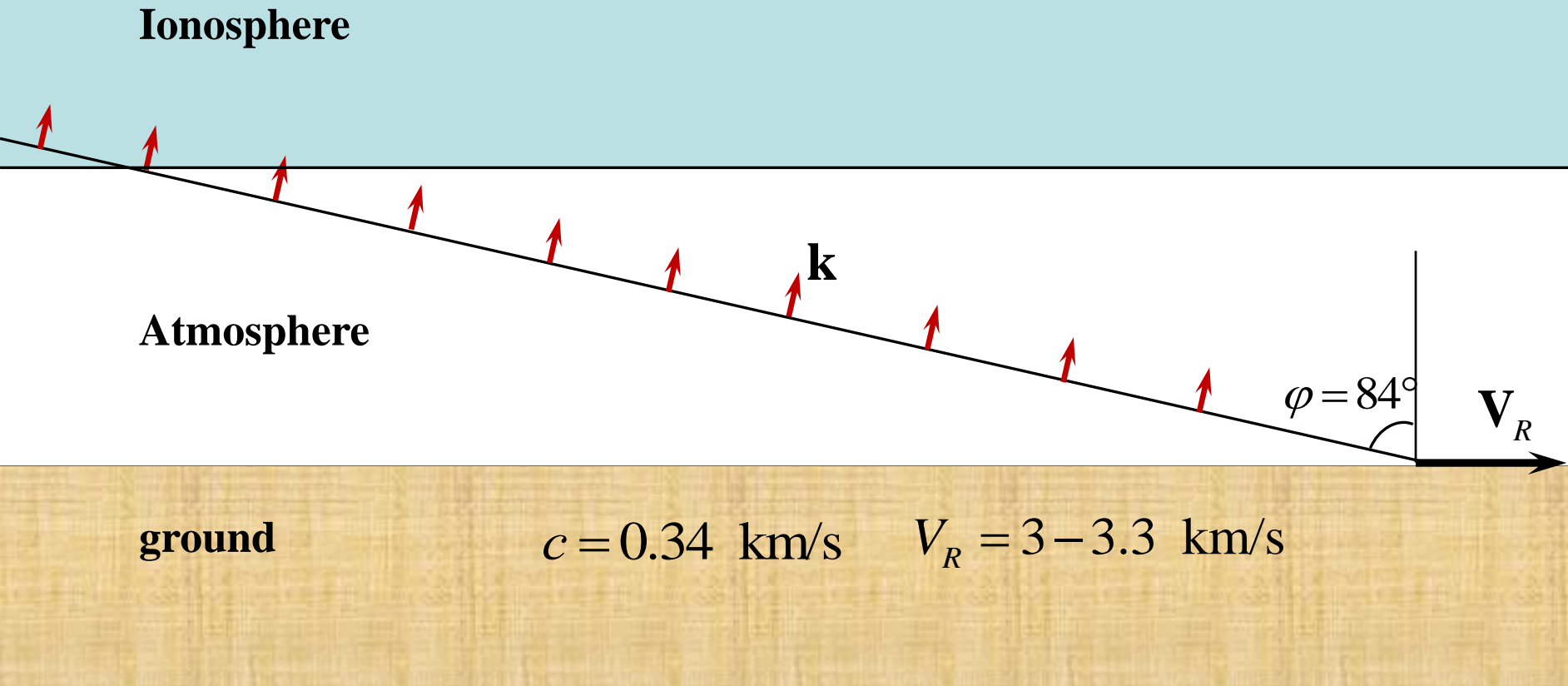


**Fig. 35.**

Whence it follows that  $k_1 \approx 2\pi/(V_R T) \approx 9 \cdot 10^{-7} \text{ cm}^{-1}$ ,  $\alpha = 1/(2H) \approx 6 \cdot 10^{-7} \text{ cm}^{-1}$  and  $M = V_R/c = 9 - 10$ . Under such conditions, acoustic waves with a wave vector directed almost vertically are excited. In this case, the angle  $\varphi$  between wave vector  $\mathbf{k}$  and horizontal axis is equal to  $84^\circ$ . The calculated pressure value for these parameters is 4.5 Pa.

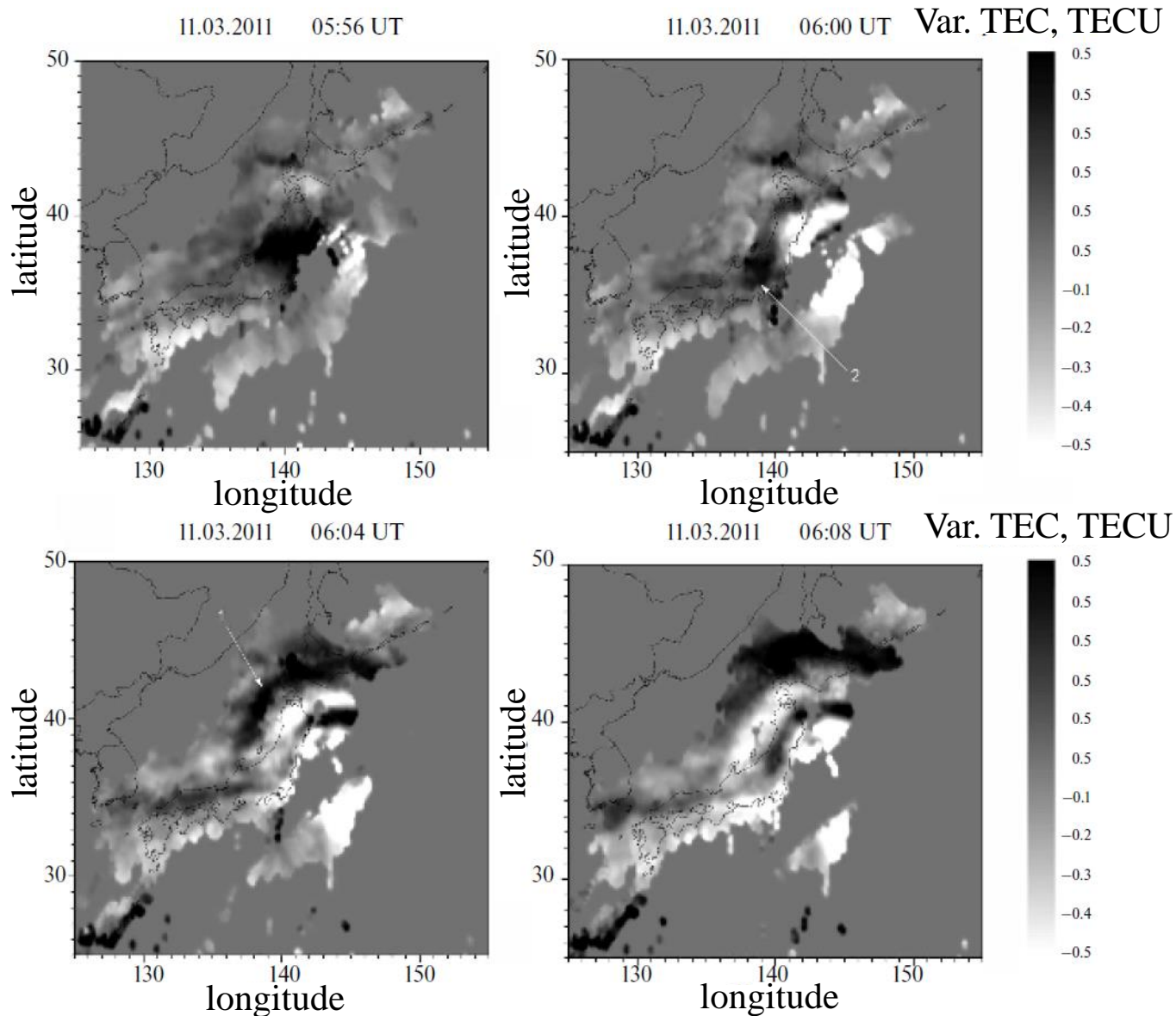


**Fig. 36.** The beginning of the generation of ionospheric disturbances by acoustic waves from an earthquake (shown by arrow 1) and a seismic Rayleigh wave (shown by arrow 2). At the top of each fragment, a date and a universal time (UT) are indicated. The scale of TEC variations is shown on the right [Kunitsyn et al., 2011; Shalimov et al., 2019].

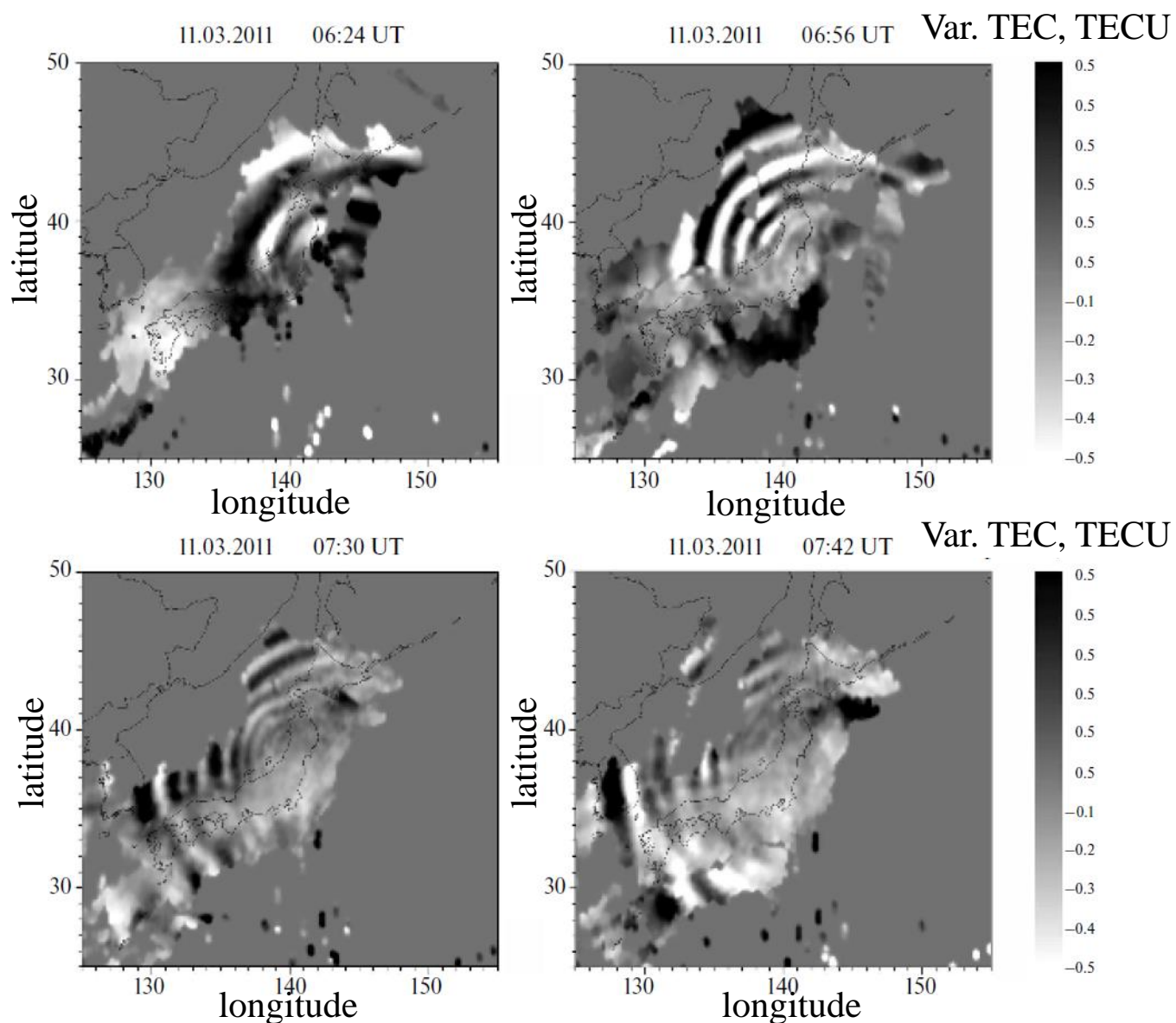


**Fig. 37.** Ionospheric disturbances at subsequent moments of time (the designations are the same as in Fig. 36): evolution and attenuation of a divergent ring disturbance caused by acoustic-gravity waves generated by an earthquake [Kunitsyn et al., 2011; Shalimov et al., 2019].

# 4. Atmospheric effects due to gas and aerosols emission from soil

## 4.1. Radon effect on the atmospheric conductivity

The nuclei  $^{222}_{86}\text{Ra}$  are effective sources of air ionization because their half-life is 3.82 days. The decay of one radon nucleus leads to the formation of  $10^5$  pairs of ions.

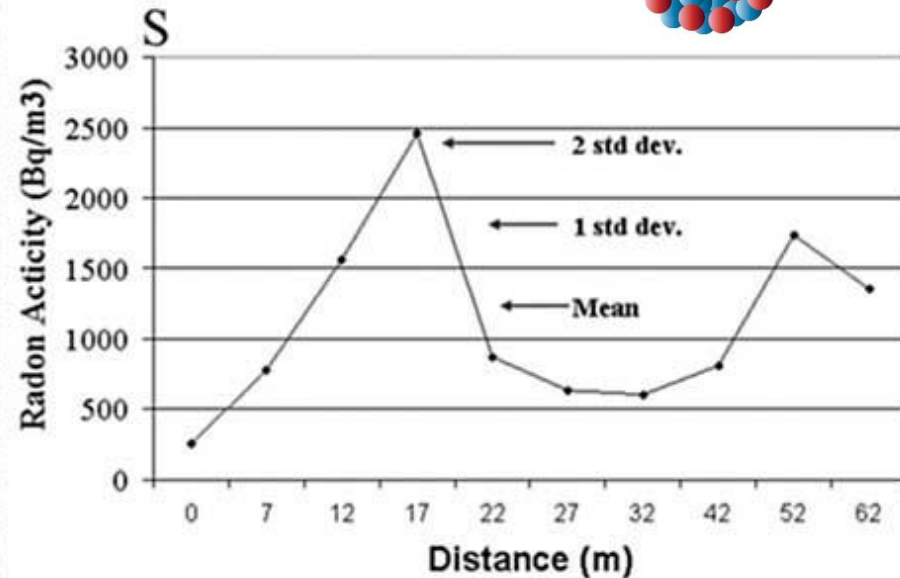
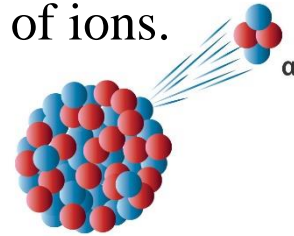
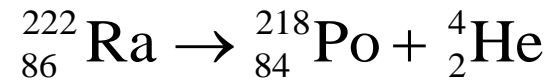
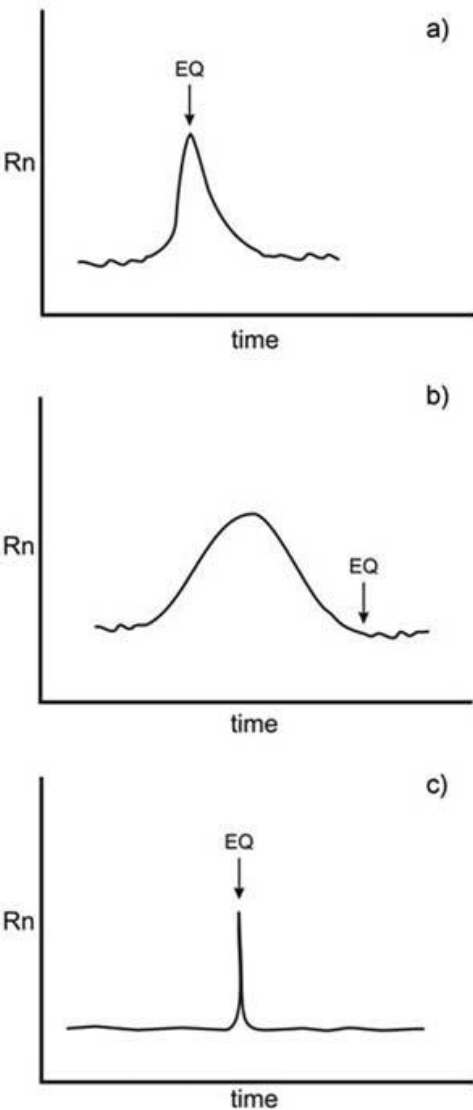


**Fig. 38.** Spot soil gas radon measurements conducted along a profile perpendicular to a suspected fault trace for determination of best site for continuous radon monitoring station. Heavy dashed line depicts the suspected fault [Inan et al., 2008].



a) Yasuoka et al. (2009) observed a gradual increase in the concentration of atmospheric radon 2 months prior to the earthquake in Kobe (January 17, 1995;  $M_w=6.9$ ). Just before the earthquake onset, the radon activity was 2 times higher ( $20 \text{ Bq/m}^3$ )

than the average level [e.g., Virk and Singh, 1994; Giuliani and Fiorani, 2009; Yasuoka et al., 2009].

**However, a few researchers do not find statistically significant changes in the radon concentration before earthquakes [Geller 1997; Inan et al., 2008; Pitari et al., 2014; Cigolini et al., 2015].**

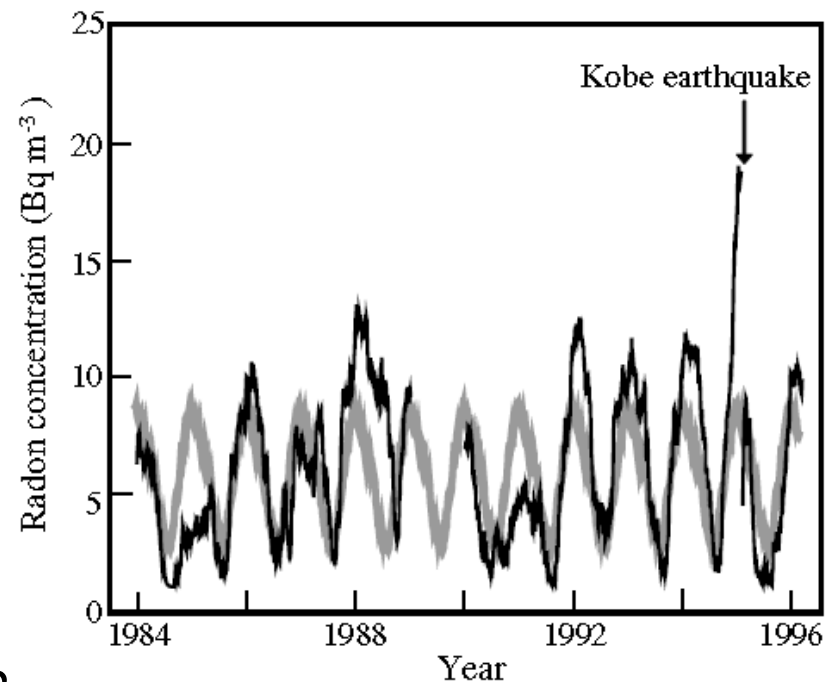


**Fig. 40**

**Fig. 39.** An example of time variation of radon data from a continuous soil gas radon monitoring site prior to (a) nearby earthquakes (150 km) with  $4.0 < M < 5.3$ , (b) close earthquakes ( $< 60 \text{ km}$ ) with  $4.0 < M < 5.3$ , (c) distant earthquakes ( $> 150 \text{ km}$ ) with magnitude between 4.0 and 5.3. [Inan et al., 2008].

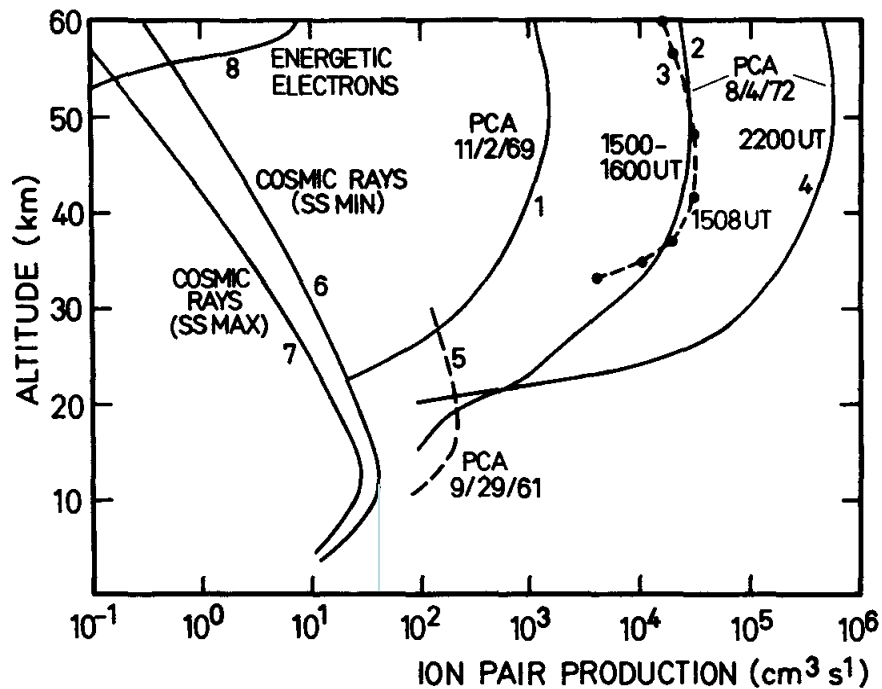


**Fig. 39.** Ion production rate in the atmosphere as a function of altitude below 60 km. [Thomas L., Radio Sci., 9, 121. 1974]

At altitudes from several km to 50–60 km, the ion production is mainly due to cosmic rays.

Near the Earth's surface, cosmic rays produce 1.5–1.7 pairs of ions/ $\text{cm}^3 \text{s}$ , whereas radon decay produces 8–10 pairs of ions/ $\text{cm}^3 \text{s}$ .

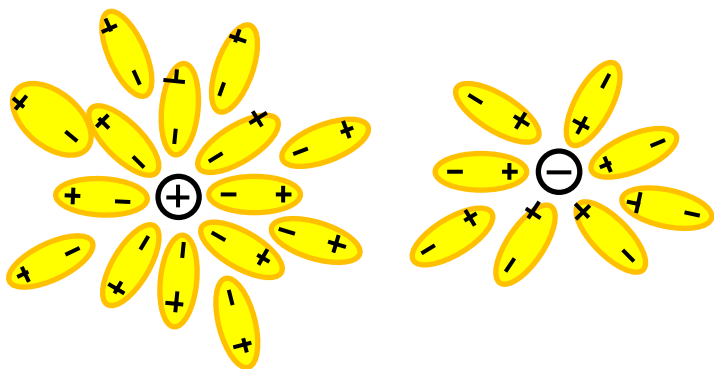


**Fig. 40.**

On the average, 10-20 neutral molecules are held around each positive ion while a negative small ion contains 5-10 neutral molecules [e.g., Tverskoy, 1962; Chalmers, 1967; Israël; 1970].

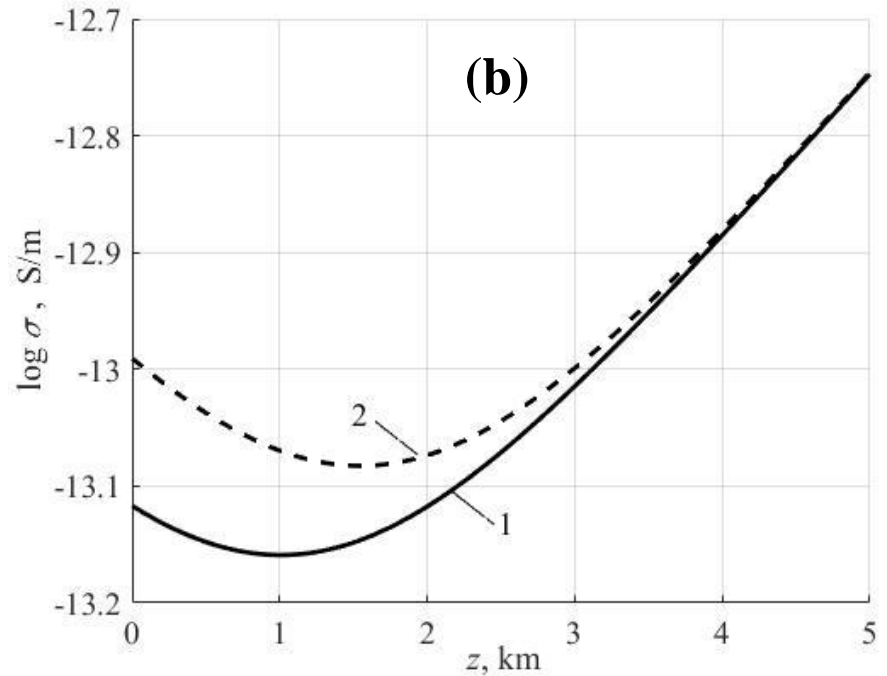
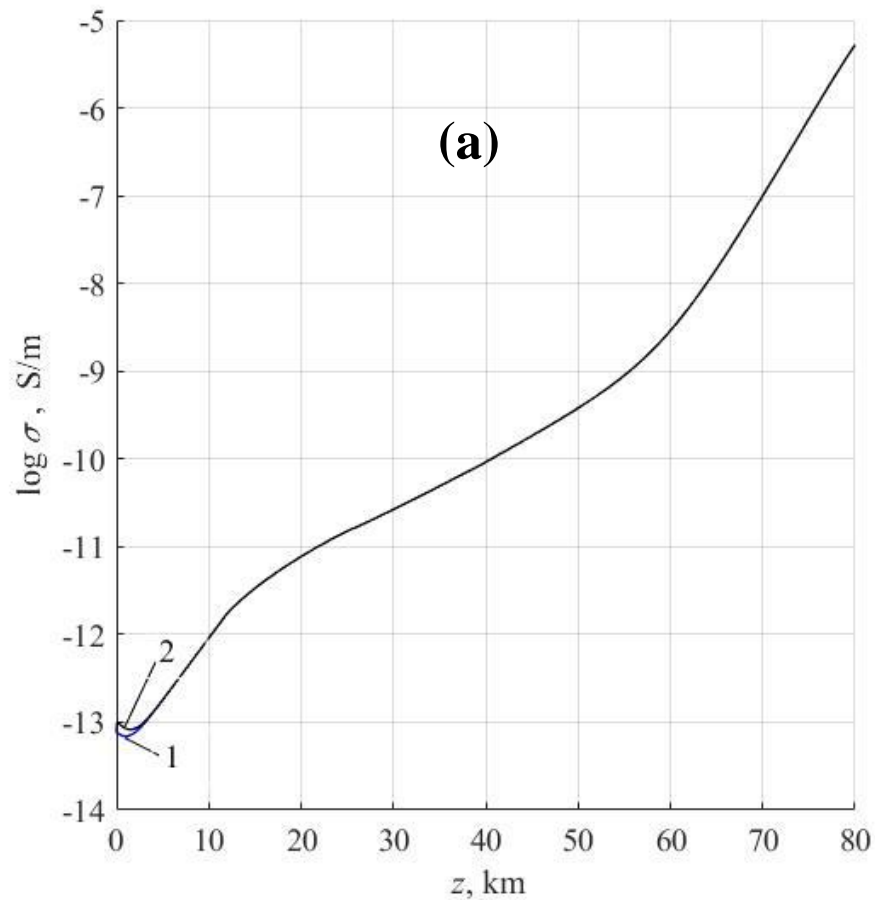
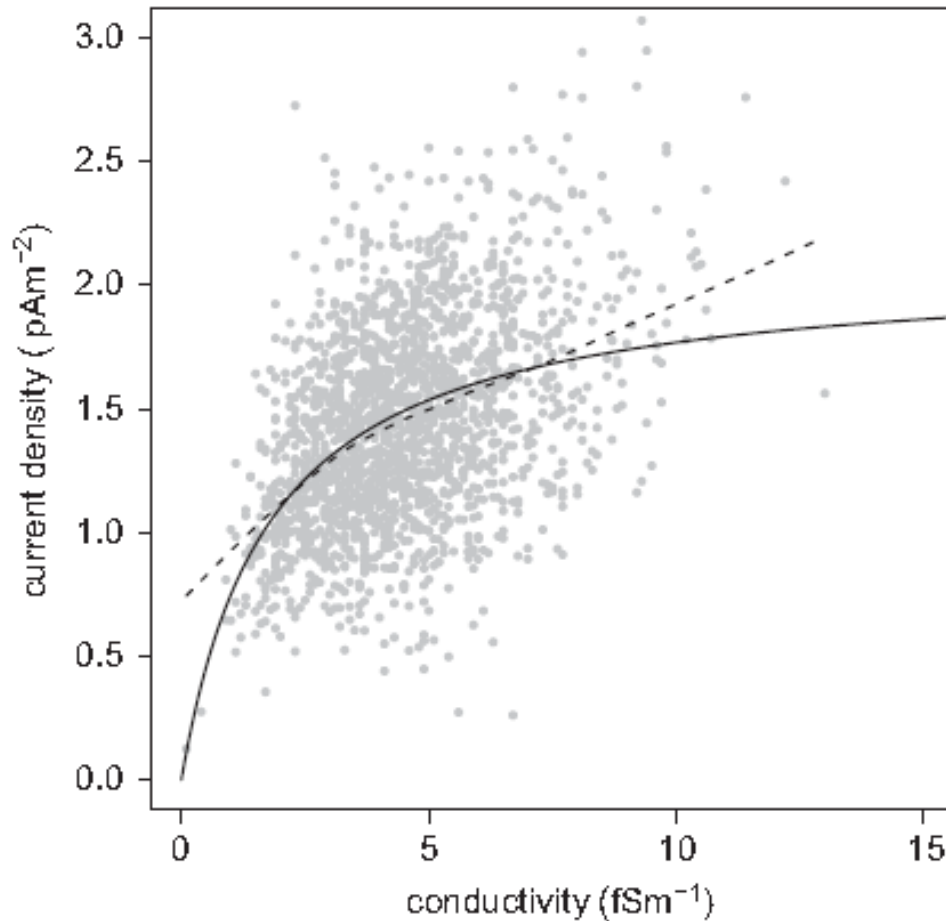


**Fig. 41.** The effect of radon emission from the soil on the electrical conductivity of the atmosphere as a function of altitude for daytime conditions. Lines 1 and 2 correspond to  $\gamma_{0r} = 6$  and  $\gamma_{0r} = 12 \text{ cm}^{-3}\text{c}^{-1}$ , respectively. (b) The initial section of the same dependence, represented on a larger scale [Surkov, 2015].

**An increase in radon activity before earthquake occurrence can cause a decrease in the resistance of the near-surface atmospheric layer by 15% for clean air and by 25% for dusty air [Harrison et al., 2010; Surkov, 2015].**



**Whether the radon concentration variation is a plausible precursor of impending earthquake or not is still an open question.**



**Fig. 42.** Daily fair weather measurements made at Kew over 14 years, of the conduction current density  $j_s$  and air conductivity  $\sigma_s$ . These were derived from independent Wilson apparatus measurements of  $j_s$  and the potential gradient, using Ohm's law. A locally weighted fit line is shown with dashed line [Harrison et al., 2010].

## 4.2. Abnormal IR radiation from the atmosphere observed above seismo-active regions

Atmospheric transparency windows 3–5  $\mu\text{m}$  and 8–13  $\mu\text{m}$ . The Earth's temperature: 273–373 K  $\Rightarrow \lambda=7.7\text{--}10.5 \mu\text{m}$ . The sizes of abnormal areas are Kopetdag 30 $\times$ 500 km, Karatau 50  $\times$ 300 km.

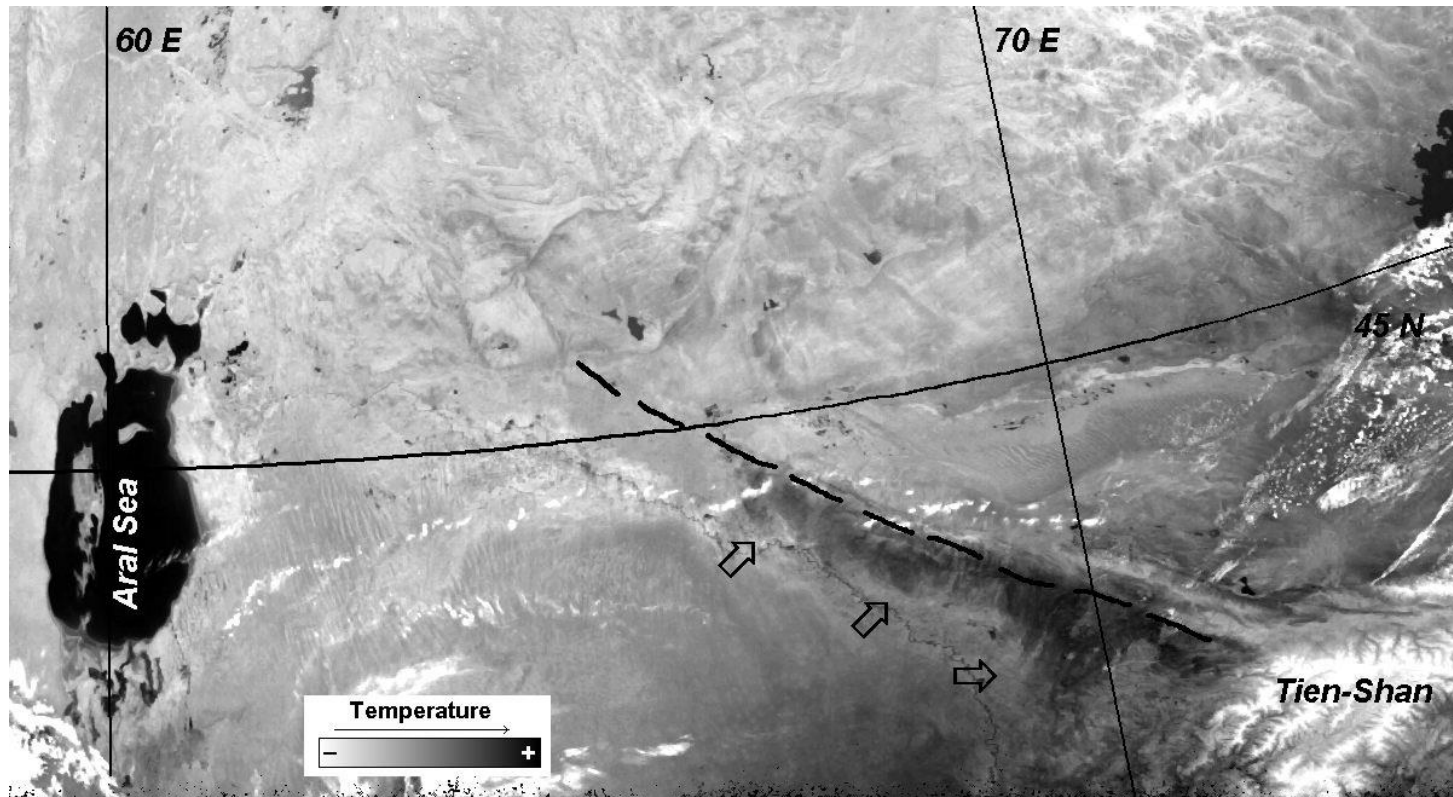
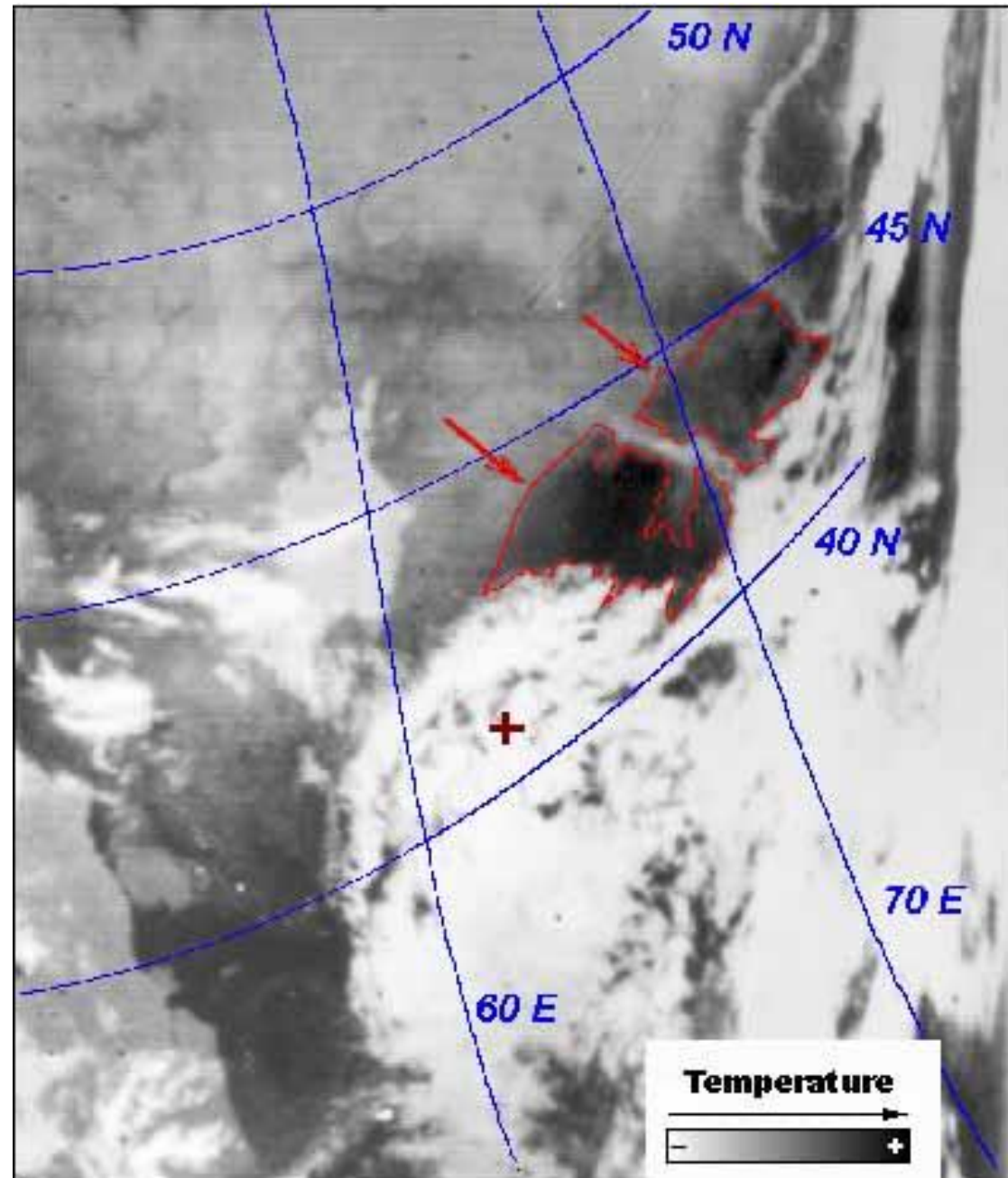


**Fig. 43.** Images of thermal IR radiation according to NOAA series satellites. The arrows show thermal "stationary" anomalies near the Karatau fault [Tronin, 1999].

Non-stationary temperature anomalies ( $\Delta T = 2.5$  K) occur near the intersection of several large faults of the Earth's crust.

**Fig. 44.** Images of thermal IR radiation 3 hours before the earthquake in Gazli (8.04.1976,  $M = 7.3$ ). The arrows show thermal anomalies; the cross indicates the epicenter of the earthquake [Tronin, 1999].



15

Long[°E]

Lat[°N]

41

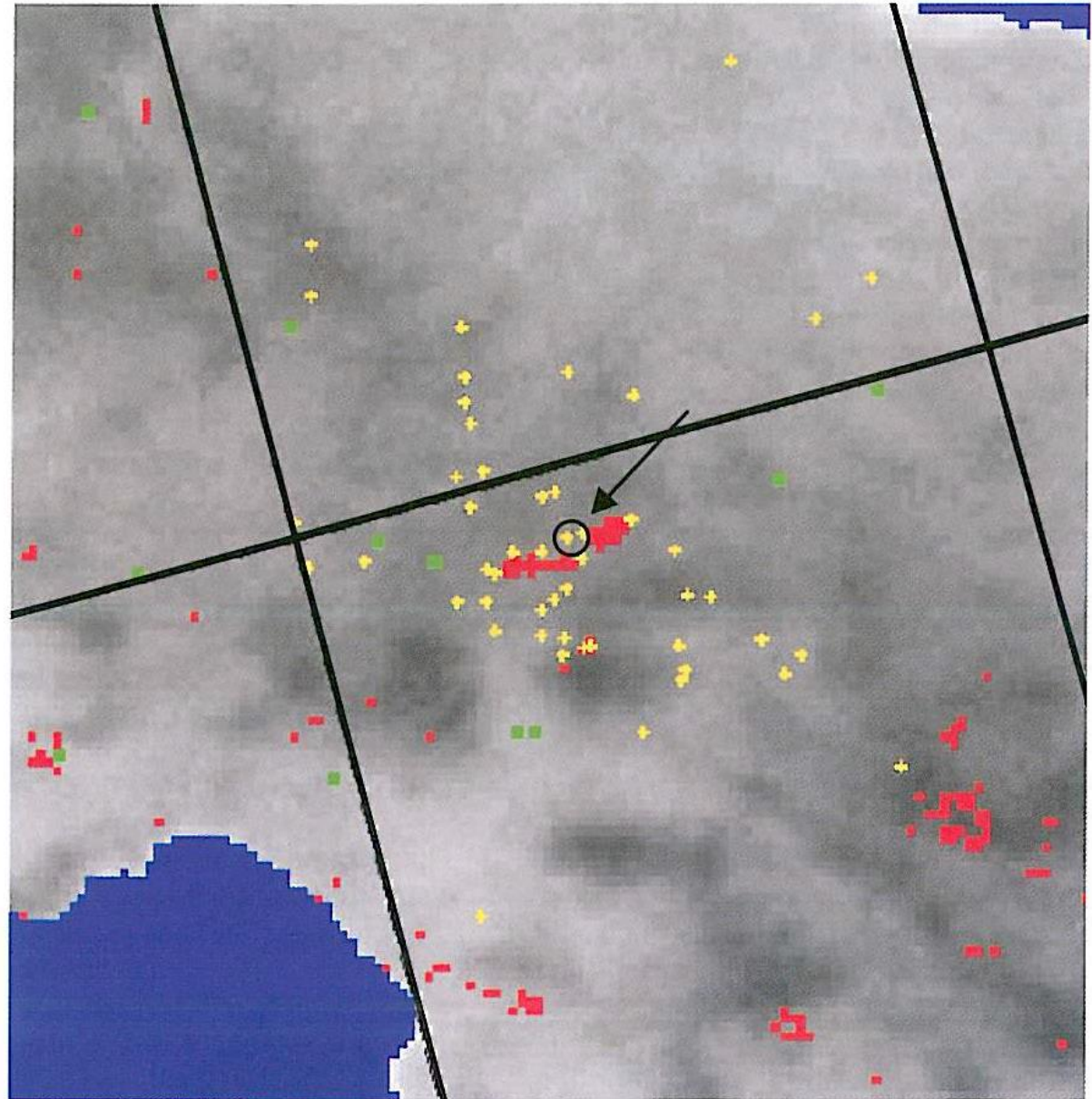


**Fig. 45.** Irpinia-Basilicata earthquake ( $M_s=6.9$ , November 23, 1980): spatial distribution of the average index of temperature anomaly (ITA) over area around the epicenter (circled) for November 1980. Yellow crosses indicate aftershocks position; green symbols localize spring sources. Pixels with  $ITA > 1.5$  are depicted in red [Tramotoli et al., 2001].

The abnormal behavior of such an area is assumed to be due to an output of optically active gases such as  $\text{CO}_2$ ,  $\text{CH}_4$ , and water vapor which results in the local green house effect [Tronin 1999].

| The main greenhouse gases of the Earth's atmosphere |                      |                  |
|---|----------------------|------------------|
| Gas   | Chemical formula     | Contribution (%) |
| Water vapor   | $\text{H}_2\text{O}$ | 36 — 72 %        |
| Carbon dioxide                                      | $\text{CO}_2$        | 9 — 26 %         |
| Methane   | $\text{CH}_4$        | 4 — 9 %          |
| Ozone   | $\text{O}_3$         | 3 — 7 %          |

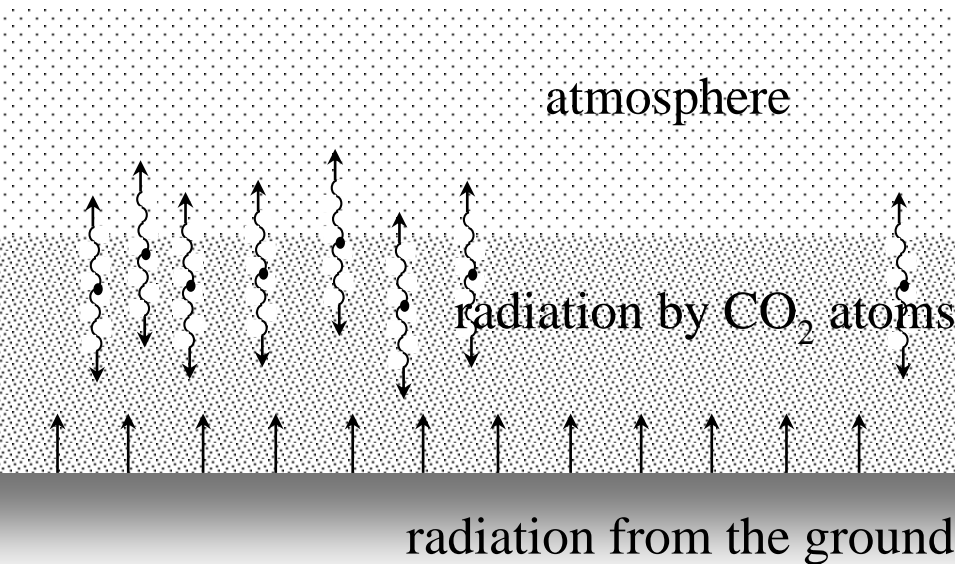


**Fig. 46.** Model of the greenhouse effect due to resonance IR absorption and radiation by the atoms of optically active gases emitted prior to earthquake. [Tronin, 1999].

## Convective heating of the ground surface caused by groundwater lifting

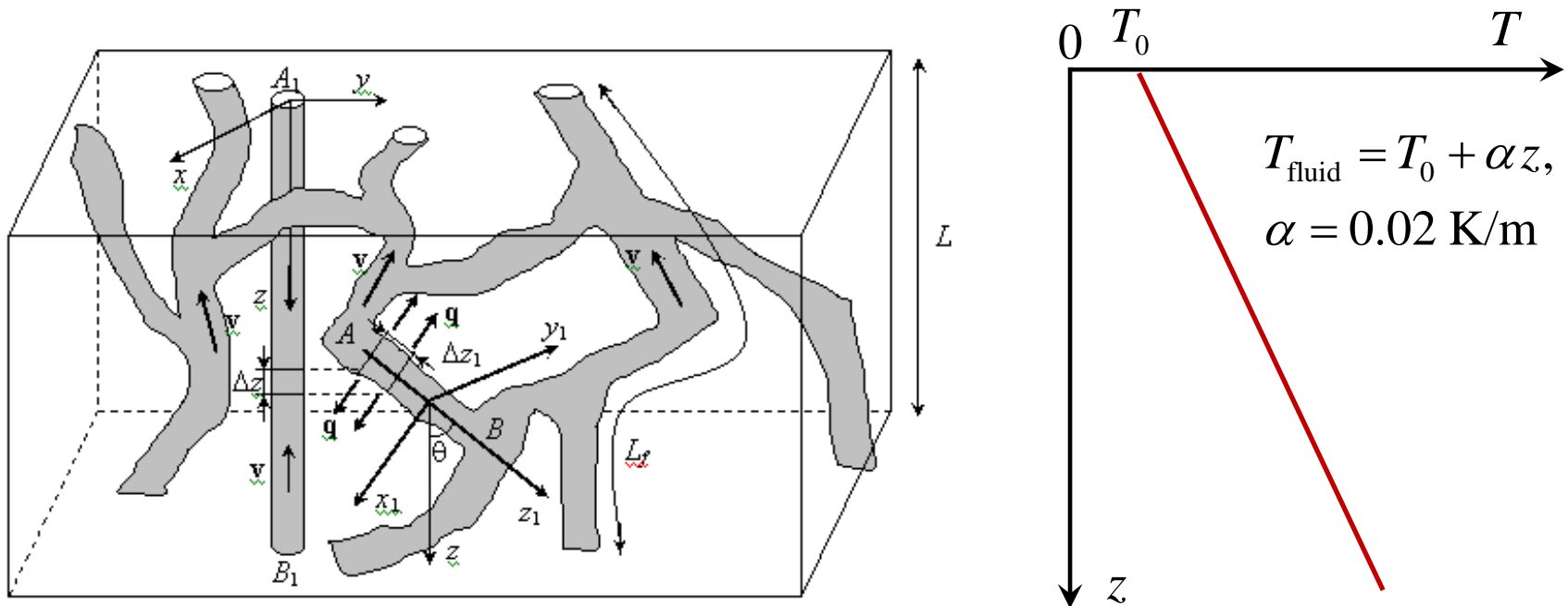


**Fig. 47.** One more plausible explanation of this phenomenon is a gradual squeezing-out of the groundwater from higher depth towards the ground surface that results from the variations of the tectonic stress in the fault zone. On the average, the ground temperature increases with depth by 2 K per 100 m that leads to the convective heating of the ground surface by a few Kelvin [Surkov et al., 2006].

If  $V_{\text{fluid}} = 8.6 \text{ cm/day}$  then  $\Delta T \approx 10^5$  years.

# 5. Ionospheric effects due to gas and aerosols 45

## emission from soil

### 5.1. Whether the radon emission from soil can heat up the atmosphere?

The hypothesis by Pulinets and Ouzounov (2011) is based on the assumption that an increase in air ionization in the surface atmospheric layer, associated with an increase in the radon concentration, will cause an increase in the intensity of water vapor condensation, which in turn will lead to the release of heat of vaporization and an increase in air temperature.



$\Delta N_r$  is the number of decayed radon nuclei;  $A = \Delta N_r / (\Delta t \Delta V)$  is radon activity;  
 $\Delta N_i = \Delta N_r n_i$  is the increase in the number of pairs of ordinary ions, where  $n_i$  is the number of pairs of ordinary ions arising from the scattering of one alpha particle in the air;  
 $\Delta N_w = \Delta N_i n_w$  is increase in the number of  $H_2O$  molecules including in light ions,  
 $n_w$  is average number of  $H_2O$  molecules attached to a cluster ion;  
 $\Delta E = \Delta N_w E_1$  is the energy released due to the molecule attachment to cluster ions;  
 $E_1$  is the energy released due to a single act of attachment;  
 $q_{\max} = \Delta E / (S \Delta t) = A n_i n_w h_r E_1$  is the maximum density of the heat energy flowing up,  
 where  $h_r$  is the thickness of the surface atmospheric layer, which contains radon atoms.

$$E_1 = \lambda M_{\text{H}_2\text{O}} / N_A = 6.8 \cdot 10^{-20} \text{ J}$$

$\lambda$  is specific heat of water vaporization and condensation;

$M_{\text{H}_2\text{O}}$  is mass mol of  $\text{H}_2\text{O}$ ,  $N_A$  is Avogadro number.

$$A = 20 \text{ Bq/m}^3, \quad n_i = 5 \cdot 10^5 \text{ pairs of ions}, \quad n_w = 10, \quad h_r = 1 \text{ m}$$

From here we obtain the maximum estimate of the upward flow density of thermal energy [Surkov, 2016]

$$q_{\max} = A n_i n_w h_r E_1 \approx 0.7 \cdot 10^{-11} \text{ W/m}^2$$

**This estimate is 12 orders of magnitude less than the estimate of the heat flow ( $q_{\max} = 16 \text{ W/m}^2$ ), which was obtained by Pulinets and Ouzounov (2011).**

The diameter of water molecule is  $d_w = 0.29 \text{ nm}$ ,  $\Rightarrow D \approx d_w n_w^{1/3} \approx 1 \mu\text{m}$

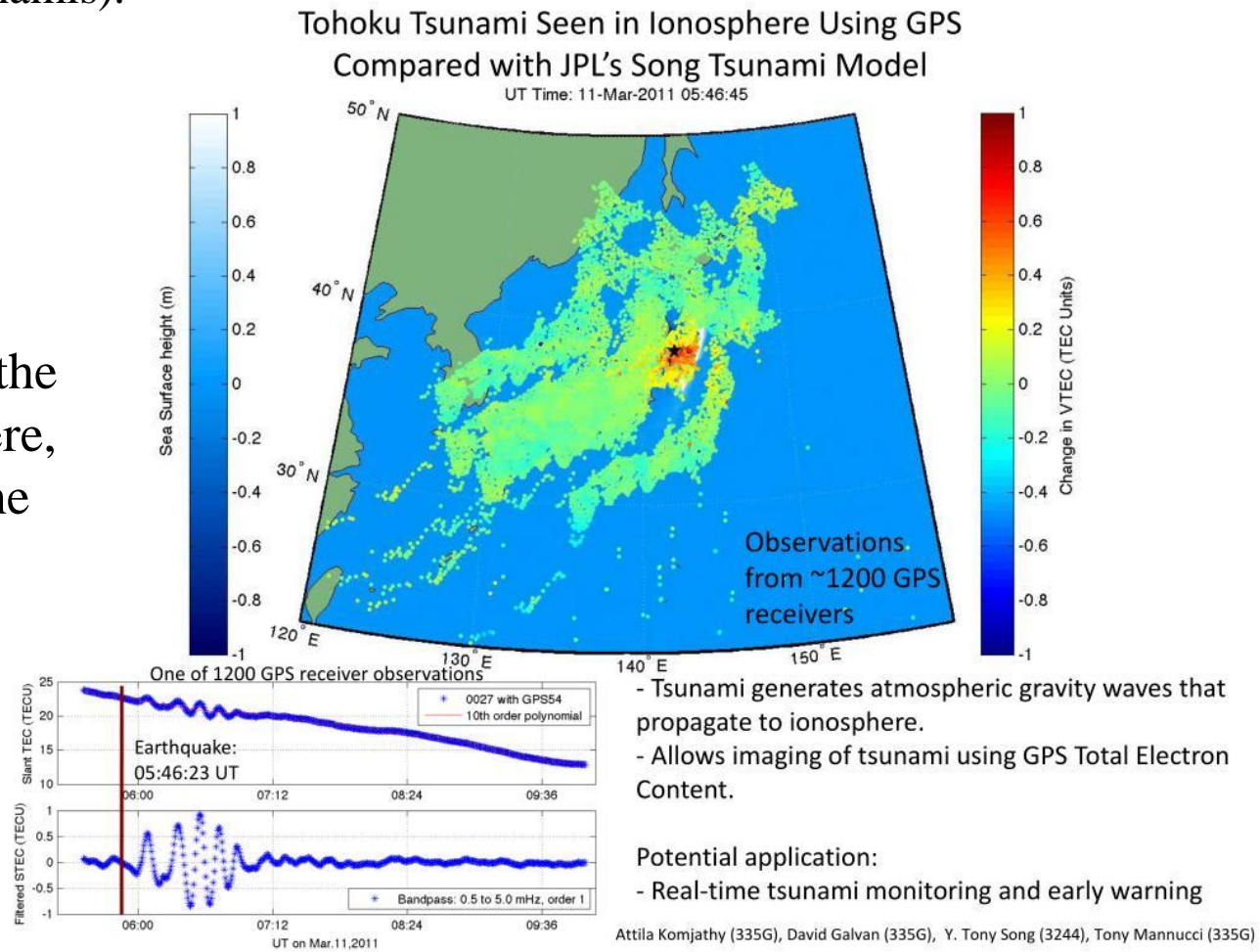
Big ion cluster,  $a \approx 1 \mu\text{m}$ .  $\Rightarrow a \approx D$ . **This is another contradiction.**

**Thus, the theoretical estimates do not confirm the hypothesis about radon heating of the lower layers of the atmosphere.**

## 5.2. Whether seismogenic atmospheric current can have an effect on the ionosphere?

The constantly expanding capabilities of GPS monitoring systems provide us information about the variations of the integral ionospheric parameter such as the Total Electron Content (TEC). At the time being the GPS/TEC observations are a global method for monitoring the propagation of acousto-gravity waves (AGW) and transients along the ionosphere and even along the Earth's surface (seismic waves, tsunamis).

**Fig. 49.** In this study it is assumed that the tsunami wave generates AGW in the atmosphere and ionosphere, which in turn results in the changes in TEC in the ionosphere.



It was hypothesized by Ouzounov et al. (2011) and Nenovski et al. (2015) that variations in radon emission before earthquakes can result in changes in the electron density in the ionosphere.

**However, according to our preliminary estimates, this effect is small** (Surkov and Pilipenko, in press):

$$\left( \frac{\delta n_e}{n_e} \right)_{\max} \sim \frac{\delta(\text{TEC})_{\max}}{\text{TEC}} \simeq \frac{\delta J_{\max}}{2\alpha e l n_e^2} \frac{\sigma_{iP}}{\sigma_P} \sim 6 \cdot 10^{-5}$$

Here  $\delta J_{\max}$  is variation of the background atmospheric current density caused by radon emission ( $\delta J_{\max} \approx 0.5 J_a = 10^{-12}$  A);  $\alpha = 10^{-13}$  m<sup>3</sup>/s is average value of the ion recombination coefficient;  $n_e = 3.1 \cdot 10^9$  m<sup>-3</sup> is the mean electron number density;  $l = 20$  km is the thickness of the ionospheric *E* layer;  $\sigma_{iP} = 3.3 \cdot 10^{-7}$  S/m is Pedersen conductivity caused by ions while  $\sigma_P = 5.8 \cdot 10^{-7}$  S/m is total Pedersen conductivity.

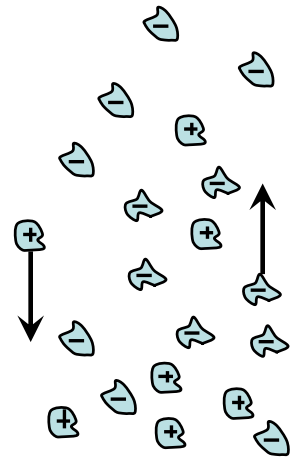
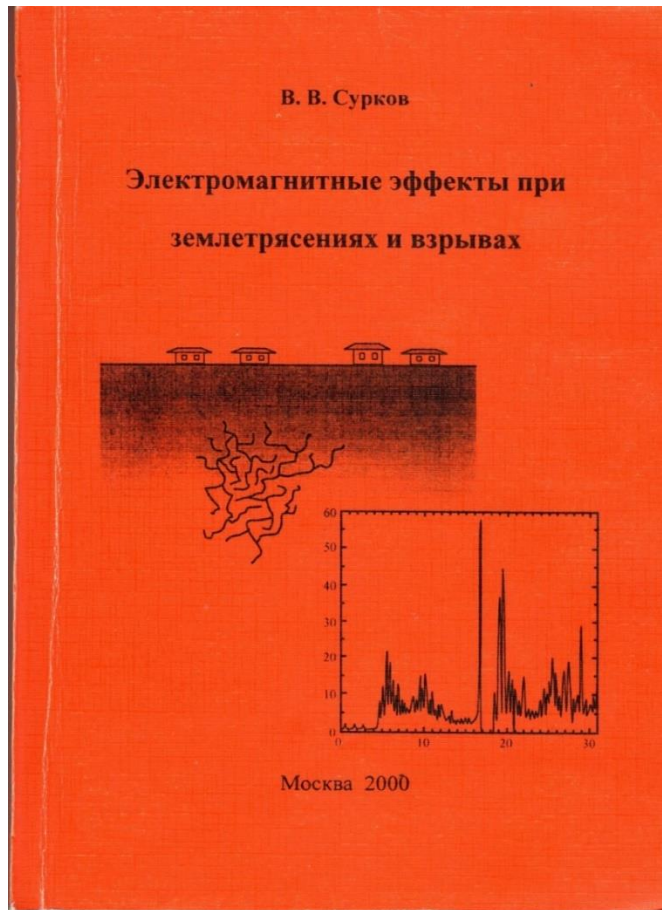
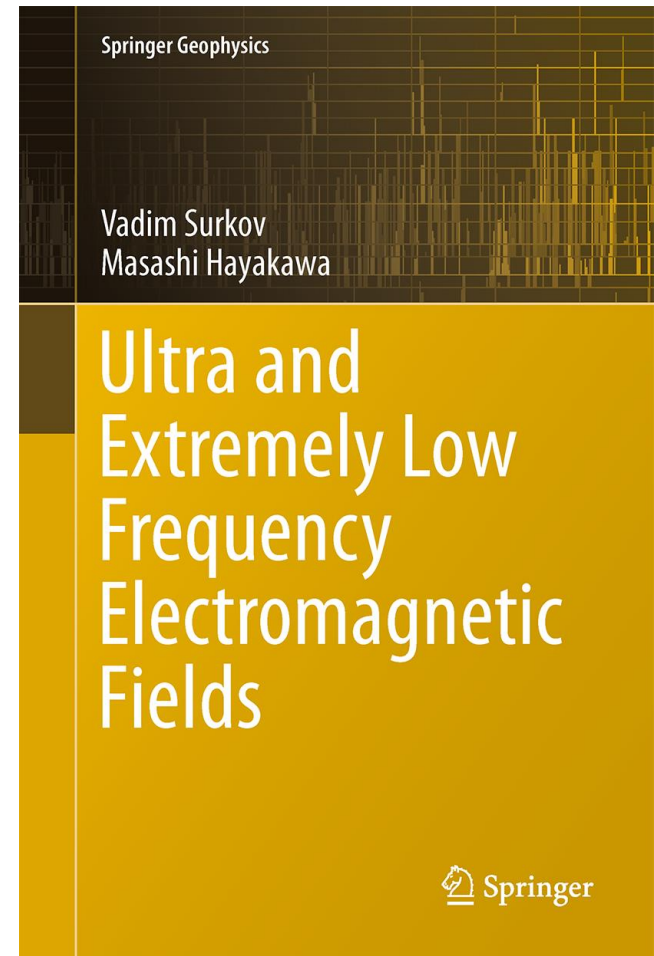


**Fig. 50.** Another hypothesis states that the occurrence of an electric field in the ionosphere over the earthquake zone is presumably associated with the vertical turbulent transfer of charged aerosols. Variations of the electric field, in turn, lead to the drift of electrons in the electric and magnetic crossed fields in the ionosphere [e.g., Pulinets and Boyarchuk, 2004; Klimenko et al., 2011; Sorokin and Hayakawa, 2014]. **Preliminary estimates show that this effect is also small.**

## 6. Conclusions



Surkov, V. V. (2000), *Electromagnetic effects caused by explosions and earthquakes*, MEPhI, Moscow, 448 pp.



Surkov, V., and M. Hayakawa (2014), *Ultra and Extremely Low Frequency Electromagnetic Fields*, Springer Geophysics Series, XVI, Springer, 486 pp.

## 1. **Local changes in the rock basement conductivity**

Can this phenomenon be used for a short-term earthquake forecast?

## 2. **Abnormal ULF electromagnetic noise possibly related to earthquakes**

It appears that ULF noise can be observed at epicenter distance no more than 100 km

## 3. **Co-seismic electromagnetic phenomena**

They are observed regularly, but these are not precursors of earthquakes!

## 4. **Atmospheric effects due to gas and aerosols emission from soil**

Radon emission seems to affect only the conductivity of the surface layer of the atmosphere.

In practice, anomalies of infrared radiation over seismically active areas cannot be observed over industrial areas and cities

## 5. **Ionospheric effects due to gas and aerosols emission from soil**

Abnormal TEC variations in the ionosphere due to these effects are very questionable

## 6. **Other effects?**

(1) Is there an effect of depression of ULF magnetic field before earthquake occurrence (Shchekotov et al. publications)? If so, how can we explain it?

(2) Are there ionospheric precursors of earthquakes? If so, how can we explain AGW generation in the ionosphere prior to earthquake occurrence?

(3) How to solve the problem of a direction finding for ULF source?

**Thank you for attention!**

